Journal of the European Ceramic Society 45 (2025) 117126

Contents lists available at ScienceDirect

Journal of the European Ceramic Society

journal homepage: www.elsevier.com/locate/jeurceramsoc

Investigating the composition-microstructure-property relationship in two dimensions in a new class of compositionally complex solid electrolytes

Shu-Ting Ko [a,b,1], Tom Lee [c,1], Jose Arturo Venegas [d], Shyue Ping Ong [a,b], Xiaoqing Pan [c,e,f,*], Jian Luo [a,b,**]

[a] Aiiso Yufeng Li Family Department of Chemical and Nano Engineering, University of California San Diego, La Jolla, CA 92093, USA
[b] Program in Materials Science and Engineering, University of California San Diego, La Jolla, CA 92093, USA
[c] Department of Materials Science and Engineering, University of California, Irvine, Irvine, CA 92697, USA
[d] Civil Engineering Department, Syracuse University, Syracuse, NY 13244, USA
[e] Department of Physics and Astronomy, University of California, Irvine, Irvine, CA 92697, USA
[f] Irvine Materials Research Institute, University of California, Irvine, Irvine, CA 92697, USA

ARTICLE INFO

Keywords:
Li-ion solid electrolytes
Compositionally complex ceramics
Microstructure
Lattice distortion
Interfaces

ABSTRACT

This study investigates the synergistic composition-microstructure-property relationships in a new class of compositionally complex perovskite oxides (CCPOs) as Li-conductive solid electrolytes. A matrix of compounds with formula $(Li_{0.375}Sr_{0.4375})(Ta_{0.75(1-y)}Nb_{0.75y}Zr_{0.25(1-z)}Hf_{0.25z})O_{3-\delta}$ (y, z = 0, 0.5, or 1) are synthesized and characterized. Correlations among composition, structural distortion, microstructure, interfaces, and ionic conductivity are systematically investigated. It is found that Nb^{5+} substitution in B sites promotes densification and grain growth, while Hf^{4+} addition expands crystal lattice, which boost interface and bulk ionic transport, respectively. Notably, $(Li_{0.375}Sr_{0.4375})(Ta_{0.375}Nb_{0.375}Hf_{0.25})O_{3-\delta}$ achieves an improved ionic conductivity of ~0.336 mS/cm, occurring concurrently with a large BO_6 distortion that enhances bulk ionic conduction and a large grain size that reduces the total grain boundary resistivity. This work represents the first in-depth experimental investigation of the composition-microstructure-property relationship of compositionally complex ceramics (CCCs) in two compositional dimensions, and it exemplifies a pathway to tailor properties in multiple compositional dimensions.

1. Introduction

The development of solid-state electrolytes (SSEs) is imperative to realize solid-state batteries (SSBs), which are intrinsically safer than conventional lithium-ion batteries and leak-free. Coupled with high-voltage cathode and Li metal anode, SSEs also enable SSBs to achieve high energy density [1,2]. Among SSEs candidates, oxide electrolytes have the advantages of excellent thermal stability, low inflammability, high transfer number, and chemical stability [3,4]. Perovskite-type solid electrolytes, specifically, present high bulk Li-ion conductivity (~1 mS/cm for $Li_{0.33}La_{0.56}TiO_3$, LLTO) and a clear conduction mechanism in ABO_3 structures through ion hopping [5,6]. However, the most well-studied LLTO is impractical for SSBs owing to its low total ionic conductivity on the order of 0.01 mS/cm, constrained by the resistive grain boundaries (GBs), as well as its poor electrochemical stability against Li metal [7]. In contrast, Ta-containing perovskite oxide $Li_{0.375}Sr_{0.4375}Ta_{0.75}Zr_{0.25}O_3$ (LSTZ) displays GB ionic conductivity in the same order as bulk ionic conductivity and improved electrochemical stability to LLTO, thereby making it a promising SSE candidate [8,9].

Recently, high-entropy ceramics (HECs) have been explored to discover new materials in a vast compositional space with the "cocktail effect" [10–12]. The synergistic cation mixing introduces chemical disorder [13,14] and structural stabilization [15,16], which further boost Li-ion conduction and maintain stability that benefits the key battery materials of anodes [17,18], cathodes [14,16], and solid electrolytes [19–22]. In a series of research efforts since 2020 [23], it was proposed to extend the materials exploration of HECs into the "compositionally complex ceramics (CCCs)" domain with non-equimolar compositions,

* Correspondence to: University of California Irvine, 644F Engineering Tower, Irvine, CA 92697, USA.
** Correspondence to: University of California San Diego, 9500 Gilman Drive, Mail Code 0448,, La Jolla, CA 92093, USA.
E-mail addresses: xiaoqinp@uci.edu (X. Pan), jluo@alum.mit.edu (J. Luo).
[1] These authors contributed equally.

https://doi.org/10.1016/j.jeurceramsoc.2024.117126
Received 23 September 2024; Received in revised form 10 November 2024; Accepted 29 November 2024
Available online 30 November 2024

enabling a broader compositional space (with continuously varying compositional variables) for tuning thermal conductivities [24], solar thermochemical water splitting efficiency [25], and Li-ion conductivities [26]. Notably, CCCs offer vast tunability in multi-dimensional compositional spaces. However, all prior studies of CCCs only investigated their properties as functions of one compositional variable, which motivates this study to further conduct an in-depth investigation of the composition-microstructure-property relationship in a two-dimensional compositional space.

Specifically for SSEs, compositionally complex perovskite oxides (CCPOs) have versatile tunability to allow multi-aliovalent doping. Extending from LSTZ, Ko *et al.* recently reported a series of CCPOs with the generic formula $(Li_{2/3x}Sr_{1-x})(Ta_{2/3x}Nb_{2/3x}Zr_{0.5(1-4/3x)}Hf_{0.5(1-4/3x)})O_{3-\delta}$ $(7/16 \leq x \leq 11/16)$ as a new class of solid electrolytes for Li-ion batteries, which showed improved phase stabilities and Li-ion conductivities [26]. In this work, we further explore a matrix of nine CCPO compositions and the baseline compounds with the generic formula $(Li_{0.375}Sr_{0.4375})(Ta_{0.75(1-y)}Nb_{0.75y}Zr_{0.25(1-z)}Hf_{0.25z})O_{3-\delta}$ (y, $z = 0$, 0.5, or 1) to investigate the compositional effects on crystal structural distortion, microstructural evolution, and Li-ion conduction in a two-dimensional compositional space for the first time.

The d^0 transition metals, such as Ta^{5+}, Nb^{5+}, Zr^{4+}, and Hf^{4+}, can distort oxide octahedrons in perovskites through second-order Jahn-Teller effects, where the empty d-orbitals of metal cations mix with the filled p-orbitals of oxide ligands [27]. The selection of d^0 cation distorters in CCPOs is examined in this work to tune the bulk ionic conductivities, which are governed by bottleneck opening through structural distortion. Moreover, the influences from each individual B-site cation and their synergistic effects on changing microstructures and GB structures are discussed. Nb-containing CCPOs generally show exaggerated grain growth behavior, which is beneficial in increasing grain sizes to reduce the effects of resistive GBs. Furthermore, a correlation analysis of two compositional variables (y and z) and measured microstructural features and properties, such as the lattice constant, mean grain size, relative density, and phase purity, provide insight into controlling B-site chemistry to change ionic conduction in the bulk phase and through interfaces. The findings can guide the composition design and property optimization beyond simple doping for discovering next-generation SSEs.

2. Material and methods

2.1. Materials synthesis

Specimens of nine different compositions, *i.e.*, $(Li_{0.375}Sr_{0.4375})(Ta_{0.75(1-y)}Nb_{0.75y}Zr_{0.25(1-z)}Hf_{0.25z})O_{3-\delta}$ (y, $z = 0$, 0.5, or 1), were synthesized via solid-state reactions similar to the conditions reported previously [26]. The stoichiometric Li_2CO_3, $SrCO_3$, Ta_2O_5, Nb_2O_5, ZrO_2, and HfO_2 precursors were ball-milled using SPEX 8000 high-energy ball mill for 100 min continuously. The powder mixture was then calcinated at 800℃ for 2 h and pelletized into 10 mm-diameter pellets at 125 MPa by a uniaxial hydraulic press. The pellets were covered by mother powders (to reduce the Li loss at high temperatures) and sintered isothermally at 1300℃ or 1200℃ in ambient air conditions for 12 h in alumina crucibles. Three Nb-rich specimens ($y = 1$) were sintered at 1200℃ (to avoid melting and reaction with crucibles) and all other six specimens were sintered at 1300℃ to achieve high densities. As reported in literature [9, 28–31], 10 wt% excess Li_2CO_3 was added on top of its nominal weight for the four endmember compositions, while there is no excess Li_2CO_3 added in CCPOs based on the optimization results reported by Ko et al. [26].

2.2. Materials characterization

2.2.1. Phase, microstructure, and Raman spectroscopy

The sintered pellets were polished and subsequently characterized by X-ray diffraction (XRD) on a Rigaku MiniFlex diffractometer with Cu K_α radiation ($\lambda = 1.5406$ Å), scanning from 20 to 80° 2θ with a scan rate of 2.3°/min and 0.01° steps. Rietveld refinement was conducted using GSASII to calculate the lattice constants ($a_{lattice}$) and quantify phase fractions of synthesized compounds. The elemental characterization was conducted by scanning electron microscopy (SEM) on a FEI Apreo with energy-dispersive X-ray spectroscopy (EDS) using an Oxford X-MAX detector. The microstructures were characterized by electron backscatter diffraction (EBSD) with an Oxford Symmetry detector at 20 kV, 13–26 nA on SEM. The grain size quantification was conducted by using the AZtecCrystal software (Oxford Instruments). Raman spectroscopy was conducted on a Renishaw inVia upright microscope with 532 nm laser source at wavenumber range of 0–1200 cm^{-1}.

2.2.2. Ionic conductivity measurement

The sintered pellets were coated by Ag paste at both sides as the blocking electrodes. The ionic conductivities were measured at room temperature by electrochemical impedance spectroscopy (Hewlett Packard 4194 A Impedance Analyzer) with frequency from 100 Hz to 40 MHz and applied voltage amplitude of 0.1 V. The impedance curves were fitted with the equivalent RC circuit models using ZView (Scribner, LLC). To obtain the activation energies of ionic conduction, the ionic conductivities were measured at elevated temperatures up to 125℃. The activation energies were calculated from the temperature dependences of ionic conductivities following Arrhenius expressions.

2.2.3. Transmission electron microscopy (TEM)

TEM sample preparation and experimental procedures are similar to what have been reported in our prior work [26]. Bulk pellets were first cut into rectangular blocks (3 mm by 2 mm in area) with the least possible thickness (typically ~0.5 mm). Then, each rectangular specimen was placed on an Allied Multiprep Polishing System, thinned, and fine-polished against diamond lapping films (Ted Pella, Inc.) of various grit sizes, performed with water. The polished ceramic was glued to a molybdenum ring (Structure Probe, Inc.) with M-Bond 610 epoxy (Vishay Precision Group, Inc.) for the subsequent ion-milling under Ar gas using a Gatan model 695 Precision Ion Polishing System.

High-angle annular dark-field scanning transmission electron microscopy (HAADF-STEM) imaging and STEM-EDS measurements were conducted using a JEOL JEM-ARM300F Grand ARM operated at 300 kV. Z-contrast HAADF-STEM imaging was performed with a probe convergence semi-angle of 25.7 mrad and large inner and outer collection angles of 70 mrad and 330 mrad, respectively. EDS spectra were acquired using the dual 100-mm^2 SDDs. Seventy-five scans (each with a 0.15-ms dwell time and 0.4 Å pixel size) in the same area at the GBs were summed.

3. Results and discussion

In this study, we designed a matrix of nine CCPO compositions following the general formula $(Li_{0.375}Sr_{0.4375})(Ta_{0.75(1-y)}Nb_{0.75y}Zr_{0.25(1-z)}Hf_{0.25z})O_{3-\delta}$ (y, $z = 0$, 0.5, or 1). The mole ratio of 5 + cations to 4 + cations is maintained as 3:1 to maintain the overall charge balance. Amongst the nine compositions, four endmembers (y, $z = 0$, or 1, denoted as LSTZ, LSTH, LSNZ, and LSNH, where L = Li, S = Sr, T = Ta, N = Nb, Z = Zr, and H = Hf), which have been studied previously [9, 29–31], were fabricated and examined to serve as our baseline. The central composition LSTNZH ($y = z = 0.5$) or $(Li_{0.375}Sr_{0.4375})(Ta_{0.375}Nb_{0.375}Zr_{0.125}Hf_{0.125})O_{3-\delta}$ was reported by Ko *et al.* [26], and four additional CCPOs (LSTZH, LSNZH, LSTNZ, and LSTNH) were fabricated, examined, and reported for the first time in this study. The chemical formulas of these nine CCPOs and their sample IDs are listed in Table 1.

Table 1
Summary of the compound formulae, synthesis conditions, and lattice constants of nine perovskite oxides fabricated in this study.

Sample ID	y	z	Nominal composition	Sintering condition	Measured lattice constant, $a_{lattice}$ (Å)
LSTZ	0	0	$(Li_{0.375}Sr_{0.4375})(Ta_{0.75}Zr_{0.25})O_{3-\delta}$	1300°C, 12 h	3.991
LSTH	0	1	$(Li_{0.375}Sr_{0.4375})(Ta_{0.75}Hf_{0.25})O_{3-\delta}$	1300°C, 12 h	4.002
LSNZ	1	0	$(Li_{0.375}Sr_{0.4375})(Nb_{0.75}Zr_{0.25})O_{3-\delta}$	1200°C, 12 h	3.991
LSNH	1	1	$(Li_{0.375}Sr_{0.4375})(Nb_{0.75}Hf_{0.25})O_{3-\delta}$	1200°C, 12 h	3.993
LSTZH	0	0.5	$(Li_{0.375}Sr_{0.4375})(Ta_{0.75}Zr_{0.125}Hf_{0.125})O_{3-\delta}$	1300°C, 12 h	3.994
LSNZH	1	0.5	$(Li_{0.375}Sr_{0.4375})(Nb_{0.75}Zr_{0.125}Hf_{0.125})O_{3-\delta}$	1200°C, 12 h	3.990
LSTNZ	0.5	0	$(Li_{0.375}Sr_{0.4375})(Ta_{0.375}Nb_{0.375}Zr_{0.25})O_{3-\delta}$	1300°C, 12 h	3.990
LSTNH	0.5	1	$(Li_{0.375}Sr_{0.4375})(Ta_{0.375}Nb_{0.375}Hf_{0.25})O_{3-\delta}$	1300°C, 12 h	3.990
LSTNZH	0.5	0.5	$(Li_{0.375}Sr_{0.4375})(Ta_{0.375}Nb_{0.375}Zr_{0.125}Hf_{0.125})O_{3-\delta}$	1300°C, 12 h	3.991

3.1. Phase formation of compositionally complex perovskite oxides (CCPOs)

We used a "powder-bed sintering" approach to cover pellets with mother powders to compensate Li loss and suppress the formation of secondary phases at high temperatures, which is commonly used in the synthesis of garnet $Li_7La_3Zr_2O_{12}$ and perovskite-type solid electrolytes [32]. The sintering temperatures are similar to the synthesis conditions for the four endmembers reported in the literature (1300°C for LSTZ [9], LSTH [29]; 1200°C for LSNZ [28]; 1250°C for LSNH [31]). Accordingly, Nb-rich group (LSNZ, LSNH, and LSNZH) was sintered at 1200°C (to avoid melting), while the rest of six samples were sintered at 1300°C.

XRD patterns of the nine specimens are shown in Fig. 1. The main phases are indexed as the cubic perovskite (space group $Pm\bar{3}m$), presented as the atomic structure model in Fig. 1(b) inset. The corresponding Rietveld refinements of lattice constants and phase fractions are shown in Fig. S1, Table 1, and Table S1. All samples show the cubic structure for the primary phase with various amounts of secondary phases identified as HfO_2/ZrO_2 [33], $LiTaO_3/LiNbO_3$ [34], $Sr_6Nb_{10}O_{30}$ [35], $SrTa_4O_{11}$ [36], and $Sr_{2.83}Ta_5O_{15}$ [37]. The formation of Li deficient strontium tantalates and strontium niobates is due to Li evaporation from the surfaces [9,28]. The presence of rhombohedral $LiTaO_3/LiNbO_3$ impurities can be attributed to the variation of Li concentration or incomplete doping of Li^+, Ta^{5+}, and Nb^{5+} into $SrZrO_3$-based framework. The deviation from stoichiometry subsequently triggers the precipitation of a HfO_2/ZrO_2 secondary phase. Based on the primary phase fractions obtained from Rietveld refinements listed in Table S1, the phase impurity level varies between 0.5 % and 6.5 % out of total crystalline phase fraction. The B-site sublattice configurational entropy (S_B^{config}) ranges from 0.56 R (four endmembers) to 1.26 R (LSTNZH), where R is the ideal gas constant (see Supporting Note S1 and Table S2). There is no clear correlation of phase stability with the value of S_B^{config} in CCPOs. Instead, the actual mole fractions of Li^+ and B-site cation species determine the phase stability, which will be discussed later in Section 3.3.

3.2. Microstructural evolution and its impact on ionic conduction

The microstructures were characterized to investigate the compositional effects on microstructural evolution. Fig. 2 demonstrates the variation of microstructures with the change of the B-site cation combination. According to the grain size quantification from electron backscatter diffraction, the baseline compounds $(Li_{0.375}Sr_{0.4375})(Ta_{0.75}Hf_{0.25})O_{3-\delta}$ (LSTH) and $(Li_{0.375}Sr_{0.4375})(Ta_{0.75}Zr_{0.25})O_{3-\delta}$ (LSTZ) show the mean grain size (d_{avg}) of 1.62 μm and 2.93 μm, respectively. While the half of Zr^{4+} sites are substituted by Hf^{4+}, d_{avg} decreases to 1.47 μm in $(Li_{0.375}Sr_{0.4375})(Ta_{0.75}Zr_{0.125}Hf_{0.125})O_{3-\delta}$ (LSTZH). Nonetheless, d_{avg} increases by 3.4 times to 10.01 μm when half of Ta^{5+} sites are

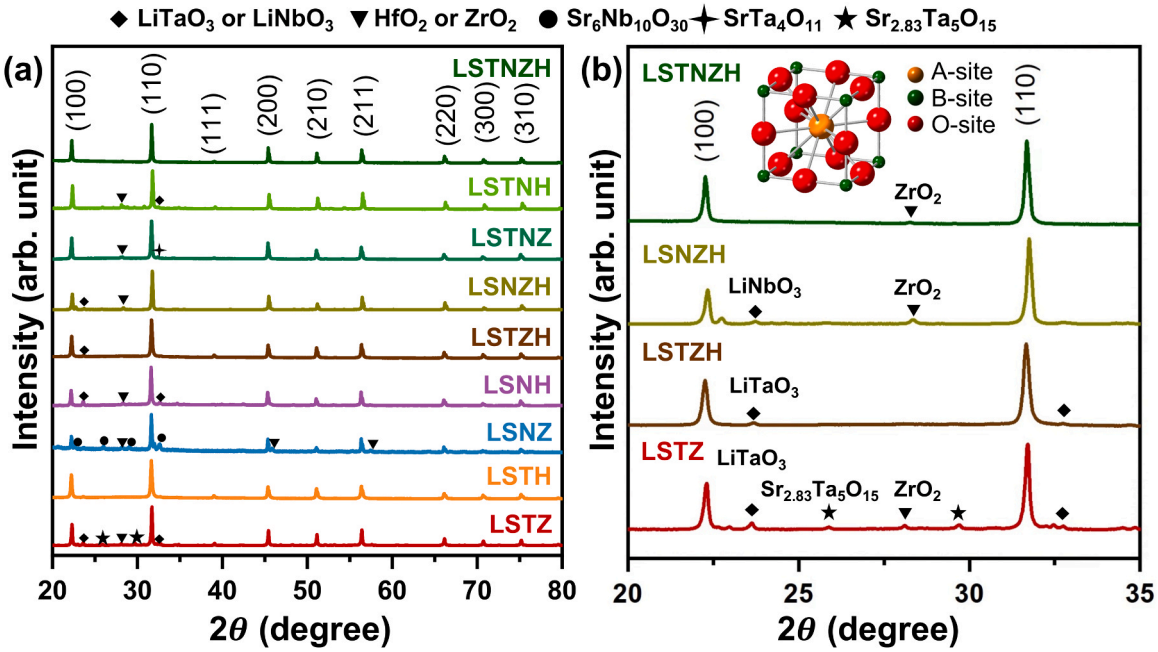

Fig. 1. (a) XRD patterns of the CCPOs with endmembers and (b) an enlarged view for four selected compositions. In panel (a), the XRD patterns from the bottom to top are those of LSTZ (red), LSTH (orange), LSNZ (blue), LSNH (purple), LSTZH (brown), LSNZH (yellow green), LSTNZ (cyan), LSTNH (light green), and LSTNZH (dark green), respectively. The XRD peaks are indexed to match cubic symmetry with the $Pm\bar{3}m$ space group. The inset in (b) presents a schematic unit cell of a cubic perovskite which consists of A-site cations at the center (orange), B-site cations (green) at the corners, and oxygens (red) at the edges.

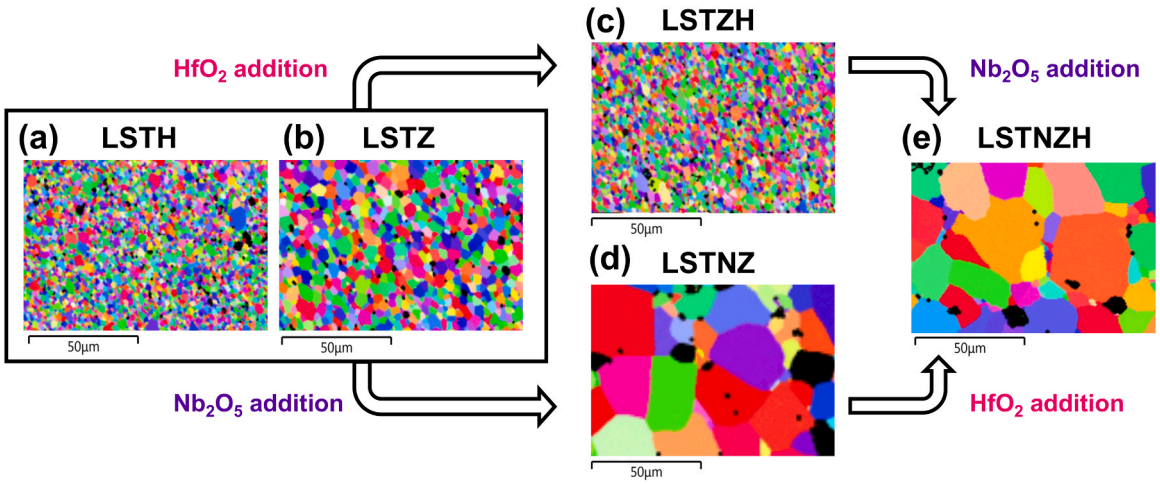

Fig. 2. Electron backscatter diffraction maps showing the variation in grain sizes upon changing the B-site chemistry of compositionally complex perovskite oxides (CCPOs), visualized by inverse pole figures along the normal direction. The EBSD maps from left to right are from (a) LSTH, (b) LSTZ, (c) LSTZH, (d) LSTNZ, and (e) LSTNZH.

substituted by Nb^{5+} in $(Li_{0.375}Sr_{0.4375})(Ta_{0.375}Nb_{0.375}Zr_{0.25})O_{3-\delta}$ (LSTNZ). The grain sizes are further increased in $(Li_{0.375}Sr_{0.4375})(Ta_{0.375}Nb_{0.375}Zr_{0.125}Hf_{0.125})O_{3-\delta}$ (LSTNZH) with a moderate increase of 7 % in d_{avg}. The three Nb-rich compositions ($y = 1$) also show large grain sizes, even though they were sintered at a lower temperature of 1200°C (*vs.* 1300°C for all other specimens). Therefore, the promotion of grain growth can be mainly attributed to the addition of Nb^{5+}.

The grain size quantification data are summarized in Table 2. Here, we note a few additional observations. Given the same Nb^{5+} occupancy, the grain sizes are smaller while Zr^{4+} cations are replaced by Hf^{4+} cations in the B sites. Thus, the grain growth is not only affected by the mole fraction of the Nb cations, but also the combination of 4 + cations. As shown in Fig. S2, LSNZ exhibits the largest d_{avg} of 13.28 μm but with irregular grain shapes and large pores, which is a result of coarsening. However, the sintering density is improved significantly (~ 96 %) in LSNZH, compared to the densities of LSNZ (~88 %) and LSNH (~88 %), at the same sintering conditions. Therefore, the fraction of 4 + cations also contributes to the change of sintering and grain growth outcomes.

The microstructure evolution was further quantified through a statistical analysis of EBSD-measured grain-size data. In Fig. 3(a-c), we present the grain size distribution histograms as a function of the grain sizes normalized with respect to the mean grain size (d_{avg}). From the top to the bottom row, Fig. 3(a-c) show the normalized grain size distributions in three groups categorized by the Nb contents as follows: (*i*) Ta-rich ($y = 0$, $X_{Ta} = 0.75$, sintered at 1300°C), (*ii*) Nb-rich ($y = 1$, $X_{Nb} = 0.75$, sintered at 1200°C), and (*iii*) mixed Nb and Ta ($y = 0.5$, $X_{Ta} = X_{Nb} = 0.375$, sintered at 1300 °C). In the Ta-rich group, LSTH shows a small d_{avg} of 1.62 μm with higher fractions of small grains ($d < d_{avg}$), whereas the grain size distribution shifts towards higher values to form a more normal distribution in LSTZ with a larger d_{avg} of 2.93 μm. When half of the Hf cations are substituted by Zr cations, the smallest d_{avg} of 1.47 μm is found in LSTZH with the grain size distribution shifts again towards lower values. In the Nb-rich group, the grain sizes are significantly larger (despite a lower sintering temperature) with wider grain size distributions, and the d_{avg} values from small to large are: LSNH (8.62 μm) < LSNZH (8.84 μm) < LSNZ (13.28 μm). These two groups show a general trend: among 4 + cations, Zr^{4+} cations promote grain growth (to result in larger grain sizes within each group). In the group of mixed Nb and Ta, the grain size distribution is broader in Zr-based LSTNZ than that in Hf-based LSTNH, where the former still shows a larger d_{avg} (10.01 μm) than that of the latter (9.82 μm). However, the mean and the standard deviation of grain sizes become even larger in LSTNZH (d_{avg} = 10.73 μm), with noticeable bimodal distribution feature that may indicate the exaggerated (abnormal) grain growth. This type of bimodal growth feature is commonly observed in perovskite oxides, such as $BaTiO_3$, $SrTiO_3$, and LLTO [38,39].

The microstructural evolution can impact properties (*e.g.*, ionic conductivity, as demonstrated in a prior study of well-studied solid electrolyte $Li_7La_3Zr_2O_{12}$) [40]. Herein, we study the microstructure-ionic conductivity correlation in CCPOs in a two-compositional-dimension space. The room-temperature impedance spectra of the three groups of CCPOs are displayed in Fig. 3(d-f). The semicircles at the higher frequency range (100 kHz) and at the intermediate range (60 kHz – 100 kHz), respectively, represent the ionic transport through the bulk and grain boundaries, respectively. Through fitting the semicircles with the brick layer model [41–43], the bulk (σ_{bulk}) and GB ionic conductivities (σ_{gb}) are calculated; see Supporting Information Note S2. The equivalent circuit model with two RC circuits in series was used for the Ta-rich group and LSTNZ, whereas only one RC circuit was employed for the Nb-rich group, LSTNH, and LSTNZH,

Table 2
Summary of the measured properties of the nine perovskite oxides.

Sample ID	Phase purity (%)	Relative density (%)	d_{avg} (μm)	d_{std}/d_{avg}	σ_{bulk} (mS/cm)	σ_{gb} (mS/cm)	σ_{gb}^{spec} (mS/cm)	σ_{total} (mS/cm)	E_a (eV)
LSTZ	93.57	87.18	2.93	0.46	0.159	0.263	9.707×10^{-4}	0.099	0.39
LSTH	99.48	97.91	1.62	0.35	0.564	0.907	2.343×10^{-2}	0.348	0.32
LSNZ	97.74	88.13	13.28	0.53	[a]	[a]	[a]	0.012	0.41
LSNH	97.33	88.16	8.62	0.51	0.055	-	-	0.055	0.42
LSTZH	99.51	87.52	1.47	0.41	0.229	0.217	1.222×10^{-3}	0.111	0.34
LSNZH	97.49	96.33	8.84	0.59	[a]	[a]	[a]	0.062	0.47
LSTNZ	97.38	93.83	10.01	0.73	0.174	0.656	1.164×10^{-3}	0.138	0.33
LSTNH	95.28	92.41	9.82	0.61	0.336	-	-	0.336	0.30
LSTNZH	98.34	95.17	10.73	0.78	0.225	-	-	0.225	0.31

[a] Bulk and GB components cannot be deconvoluted. -: The GB resistance is too small to be fitted from impedance spectra.

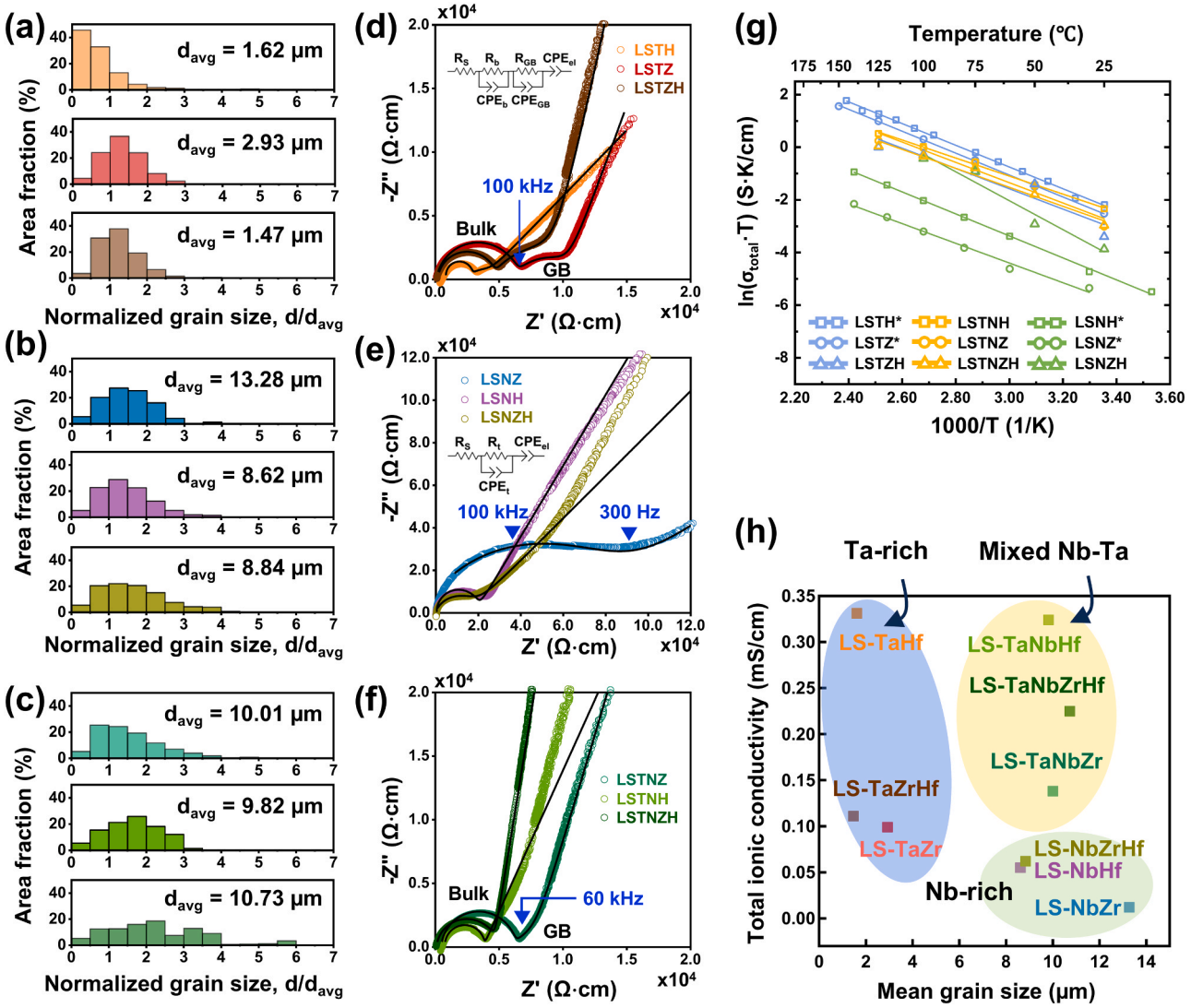

Fig. 3. The grain size distributions of (a) the Ta-rich group: LSTH (orange), LSTZ (red), LSTZH (brown), (b) the Nb-rich group: LSNZ (blue), LSNH (purple), LSNZH (yellow-green), and (c) the mixed Nb-Ta group: LSTNZ (cyan), LSTNH (light green), and LSTNZH (dark green), from top to bottom. The room-temperature impedance spectra with the fitted curves of (d) the Ta-rich group, (e) the Nb-rich group, and (f) the mixed Nb-Ta group, where the insets show the equivalent circuit models used in the fitting. (g) Arrhenius plots for total ionic conductivity from 10°C to 150°C. The Arrhenius plot data for the four reference materials LSTH [29], LSTZ [9], LSNZ [30], and LSNH [31] were from prior studies cited. (h) Nine perovskite oxides plotted in the space of the total ionic conductivity and mean grain size, grouped with shaded colors according to Ta vs. Nb contents: Ta-rich (y = 0 or X_{Ta} = 0.75, blue), mixed Ta and Nb (y = 0.5 or $X_{Ta} = X_{Nb}$ = 0.375, yellow), and Nb-rich (y = 1 or X_{Nb} = 0.75, green).

because their bulk and GB resistances could not be deconvoluted (R_{total} was fitted), or the GB resistances were too small to be fitted ($R_{bulk} \approx R_{total}$).

Among all samples, LSTH (one of four endmembers fabricated in this study as references) presents high bulk and total ionic conductivities, while all other three endmembers exhibit substantially lower ionic conductivities. Amongst the five medium-entropy CCPOs, LSTNH exhibits the highest total ionic conductivity of 0.336 mS/cm (almost identical to LSTH within the measurement errors). We shall note that the LSTH endmember fabricated in this study has a noticeably higher phase purity (>99 %) and relative density (~98 %) than those of LSTNH (~95 % phase purity and ~92 % relative density). Thus, it is likely that LSTNH can be further optimized (through further processing optimization) to achieve higher conductivity. For example, the spark plasma sintering has been used to optimize the relative density of LSTH to achieve a room-temperature ionic conductivity of 0.52 mS/cm [44], which was increased by 73 % from that of LSTH pellets made by conventional sintering in a regular box furnace [29].

In Ta-rich group (Fig. 3(d)), the bulk conductivities drop upon the incorporation of Zr^{4+} in LSTZH and LSTZ, where Hf^{4+} occupancy increases the bulk ionic conductivity. This is correlated with the increase in lattice constant values (Table 1), leading to expanding the bottleneck size for Li-ion transport. Additionally, the relative sintering density of LSTH is 97.91 %, which is significantly higher than those of LSTZ (87.18 %) and LSTZH (87.52 %), and contributed to its high total ion conductivity. In the group with mixed Ta and Nb (Fig. 3(f)), the presence of Zr^{4+} does not play a significant role in affecting the bulk conductivity when we compare LSTNH with LSTNZH. Further comparing their activation energies fitted from the Arrhenius-type plots shown in Fig. 3(g), LSTNH shows an activation energy of 0.30 eV, which is 0.01 eV lower than that of LSTNZH. In terms of microstructures, LSTNZH exhibits exaggerated grain growth with extremely large grains and broad grain size distribution. The grain growth kinetics is influenced by the change of GB chemistry and structures, which have been studied in other oxide systems [45–48]. We will further compare the GBs in LSNZH and LSTZH in Section 3.4 to reveal the role of Nb^{5+} in densification and interfacial

compositions.

Temperature-dependent ionic conductivity measurements are carried out to study the change in ionic transport behavior upon increasing temperatures from room temperature to 125℃. Fig. 3(g) depicts the corresponding Arrhenius plots with *y*-axis plotted in $\ln(\sigma_{total} \bullet T)$ and *x*-axis plotted in $1000/T$, where σ_{total} and T are the total ionic conductivity and the dwell temperature, respectively. The activation energies of ionic transport are computed from the fitted slopes of linear curves of the Arrhenius plots (as elaborated in Supporting Information Note S3). By categorizing the samples based on the molar fraction of Nb^{5+} *vs.* Ta^{5+} cations in the B site, the Ta-rich group ($y = 0$ or $X_{Ta} = 0.75$), which includes LSTH, LSTZ, and LSTZH, exhibits intermediate values of activation energies in the range of 0.32 – 0.39 eV. The mixed Ta and Nb group ($y = 0.5$ or $X_{Ta} = X_{Nb} = 0.375$), containing LSTNZ, LSTNH, and LSTNZH, shows lower activation energies in the range of 0.30 – 0.33 eV. In contrast, the Nb-rich group ($y = 1$ or $X_{Nb} = 0.75$) shows the largest activation energies of 0.41 – 0.47 eV, resulting in poorer ionic conductivities. The ionic transport differences in the three groups can largely be attributed to the change in the pre-factor, a bulk composition-dependent variable that is related the activation entropy [22,49–51].

To better illustrate the observed trends, Fig. 3(h) plots the three groups of CCPOs in the space of the room-temperature total ionic conductivity and mean grain size. The Ta-rich group is in the small grain size region with a wide range of total ionic conductivity values, whereas the Nb-rich group sits in the large grain size region with low total ionic conductivities. In between, the mixed Ta and Nb group retains the large grain sizes, where the higher Hf^{4+}/Zr^{4+} ratio leads to greater total ionic conductivity. While there are clear trends in Fig. 3(h), the total ionic conductivity does not depend solely on the mean grain size or the fraction of any particular cation. More descriptors and further analyses are required to fully unveil the composition-microstructure-property relationship.

3.3. Correlation of B-site chemistry with microstructures and properties

The interplays among composition, microstructure, and conductivity need to be evaluated. Fig. 4 visualizes the correlations of target features in the 2D compositional space, where the *x*-axis is the normalized Nb fraction, $y = X_{Nb}/(X_{Nb} + X_{Ta})$, and the *y*-axis is the normalized Hf fraction, $z = X_{Hf}/(X_{Hf} + X_{Zr})$. Herein, the four microstructural features presented in Fig. 4(a-d) are: (a) the measured mean grain size (d_{avg}), (b) the normalized grain size standard deviation (d_{std}/d_{avg}), (c) the measured relative sintered density, and (d) the measured phase purity (*i.e.*, the fraction of primary phase). The colormaps represent the magnitudes from the selected physical properties on the 2D compositional space. In addition, the bulk ionic conductivity (σ_{bulk}) and the measured lattice constant are examined as the other two features for describing crystal structure and ionic transport behavior in the bulk phase as shown in Figs. 4(e) and 4(f), respectively.

In Fig. 4(a), the mean grain size increases with increasing Nb content from for $y = 0$–0.5, and it further increases along the diagonal direction with increasing Nb and Zr contents in Nb-rich (high *y*) region. This trend illustrates the dependence of enhanced grain growth on the co-existence of Nb and Zr cations when Nb cations become dominant. Furthermore, the broadening of the grain size distribution in Fig. 4(b) shows a maximum at $y = 0.5$ and $z = 0.5$ in LSTNZH, suggesting the bimodal microstructure development in the mixed composition with the highest configurational entropy.

From the processing point of view, Nb_2O_5 has been reported as the sintering aid with a low melting point (m.p. 1512℃), which can facilitate the densification process and reduce the sintering temperature of ceramics [52,53]. This trend is observed in Fig. 4(c), where the relative

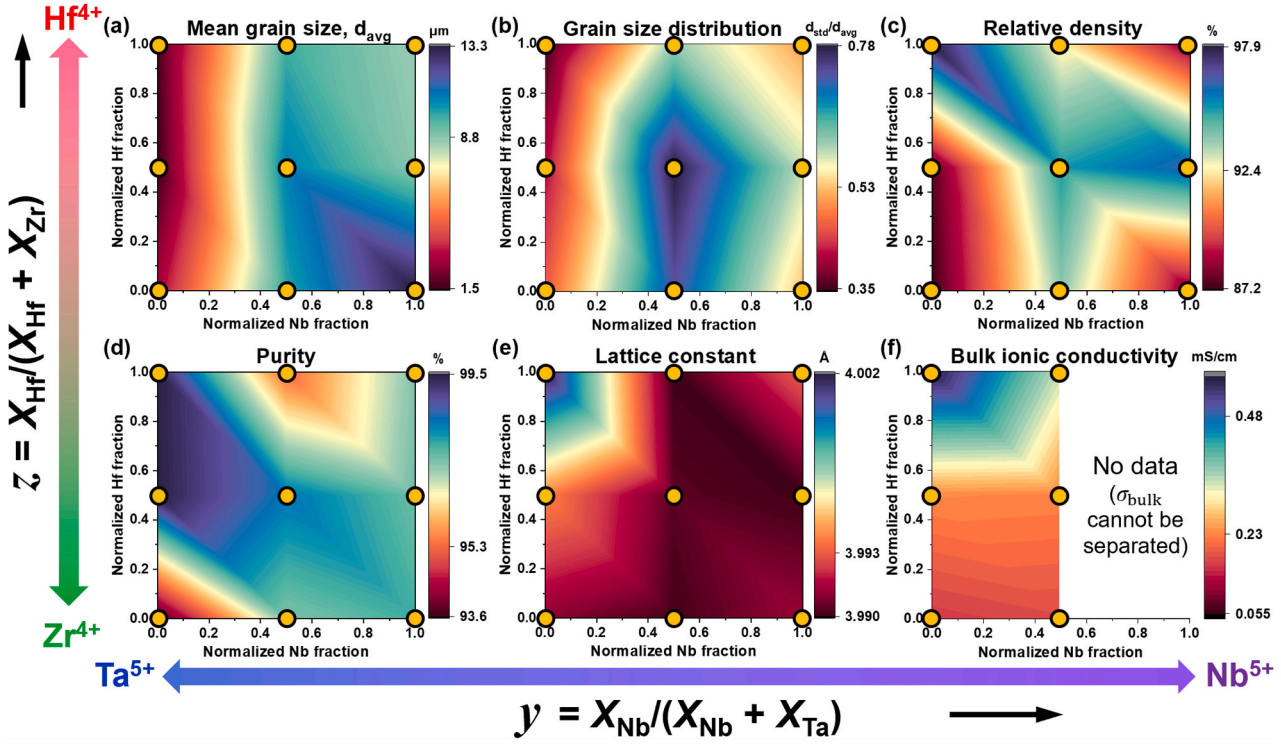

Fig. 4. The contour plots of the change in physical properties of CCPO subsets in the composition space, defined by normalized Nb fraction (y) and normalized Hf fraction (z). The experimental data points are marked as filled circles in yellow and the corresponding physical properties are color-coded from dark red (lowest value) to dark blue (highest value). (a-d) presents microstructural features: (a) mean grain size, (b) normalized grain size standard deviation, (c) relative sintering density, and (d) primary perovskite phase fraction, denoted as purity. (e) displays the lattice constants from Rietveld refinements of XRD patterns in Fig. 1, which are correlated with (f) bulk ionic conductivities. The right-half region in (f) is white as the bulk ionic conductivity cannot be separated from the impedance measurements.

sintering density is ameliorated along with the increase of the $X_{Nb}/(X_{Nb} + X_{Ta})$ when the $X_{Hf}/(X_{Hf} + X_{Zr})$ is fixed at 0.5. Yet, the porous structure is developed in LSNZ (the bottom-right point in Fig. 4(c)), which may be related to the eutectic reaction in Nb_2O_5-ZrO_2 binary phase diagram at a ratio of Nb_2O_5:ZrO_2 = 75:25 by mole [54], which may lead to poor processability (and reduced phase stability) at the controlled sintering temperature of 1200℃. In contrast, the trend is reversed at the $X_{Hf}/(X_{Hf} + X_{Zr})$ or $z = 1$, where LSTH exhibits the highest density. Hence, sinterability is not governed by any single element; instead, the combination of cations and their molar fractions plays a pivotal role. The dominant Nb^{5+} mole fraction in B sites poses more drawbacks, not only in reducing density but also in triggering phase instability. The benefit of Nb^{5+} in promoting sintering and single-phase formation is maximized when Nb^{5+} and Ta^{5+} are equimolar or $y = 0.5$, where Ta substitution leads to a higher melting temperature and stabilizes the structure.

Other than microstructural features, the bulk ionic conductivity is correlated with the lattice constant values in the upper-left corner in Fig. 4(e) and (f). The larger lattice constant of LSTH suggests the expansion of the bottleneck size for Li-ion conduction. Moreover, the lattice distortion has been reported to impact Li-ion mobility in anti-perovskites [55]. In addition, the B-site transition metal cations with d^0 orbital in perovskites, including Ti^{4+}, Nb^{5+}, and W^{6+}, can distort structures through second-order Jahn-Teller (SOJT) effects [27,56]. The spontaneous BO_6 octahedral distortions will lead to dynamic fluctuations of B-O bond lengths. The stronger B-O bonds induced from B-cations with higher valency are favorable to weaken the electrostatic potential of A-O bonds, thereby creating a facile Li-ion transport pathways with higher ionic mobility and lower activation energy [5].

In this study, we performed Raman spectroscopy, which has been demonstrated as a sensitive tool to study structural distortions and order-disorder transitions in perovskite oxides [57–60]. Raman scattering refers to the inelastic scattering of light, generated by the oscillation of induced electric dipoles subjected to incident radiation, which can provide structural information of molecules and inorganic compounds [61]. For example, the shift in the wavenumber for perovskite-type orthochromites was found to be associated with the octahedral rotation angle induced by chemical pressure, due to the difference in ionic radii in $RCrO_3$ (R = Y, La, Pr, Sm, Gd, Dy, Ho, Yb, Lu) [57]. According to group theory, an ideal cubic perovskite oxide (space group $Pm\bar{3}m$ with O_h octahedral symmetry) is infrared active but Raman inactive. Therefore, the first-order Raman scattering in vibrational spectra is only allowed in the perovskites with the loss of cubic symmetry [62], as observed in $CaTiO_3$ and complex perovskites with B-site ordering[63].

Fig. 5(a-c) shows the Raman spectra of Ta-rich, Nb-rich, and mixed Nb-Ta groups, respectively. The positive Raman shifts indicate the change in energy between incident and scattered photons, resulting from the absorption of energy by different vibrational modes in the distorted structures. Based on the structural study of $SrTi_{1-x}Sn_xO_3$ by Lavinscky *et al.* [59], the Raman responses in the range of (*i*) 150 and 500 cm^{-1} corresponds to the vibration modes from coupled A- and B-cation sublattice (200–300 cm^{-1}) and bending of B-O bonds (300–400 cm^{-1}). The shifts between (*ii*) 500–800 cm^{-1} involves BO_6 octahedral bending (500–600 cm^{-1}) and stretching modes in [111] distortion (600–800 cm^{-1}). Accordingly, the three major Raman shift peaks in the spectra are assigned as $\Delta\nu_1$ (200–250 cm^{-1}), $\Delta\nu_2$ (588–602 cm^{-1}), and $\Delta\nu_3$ (845–880 cm^{-1}) in Fig. 5(a-c). The peaks below 200 cm^{-1} become pronounced in LSNZ and LSNH, which can be the specific mode from B-cation sublattice due to the change of B-site cation species, or from local secondary phases. Similarly, the additional peaks

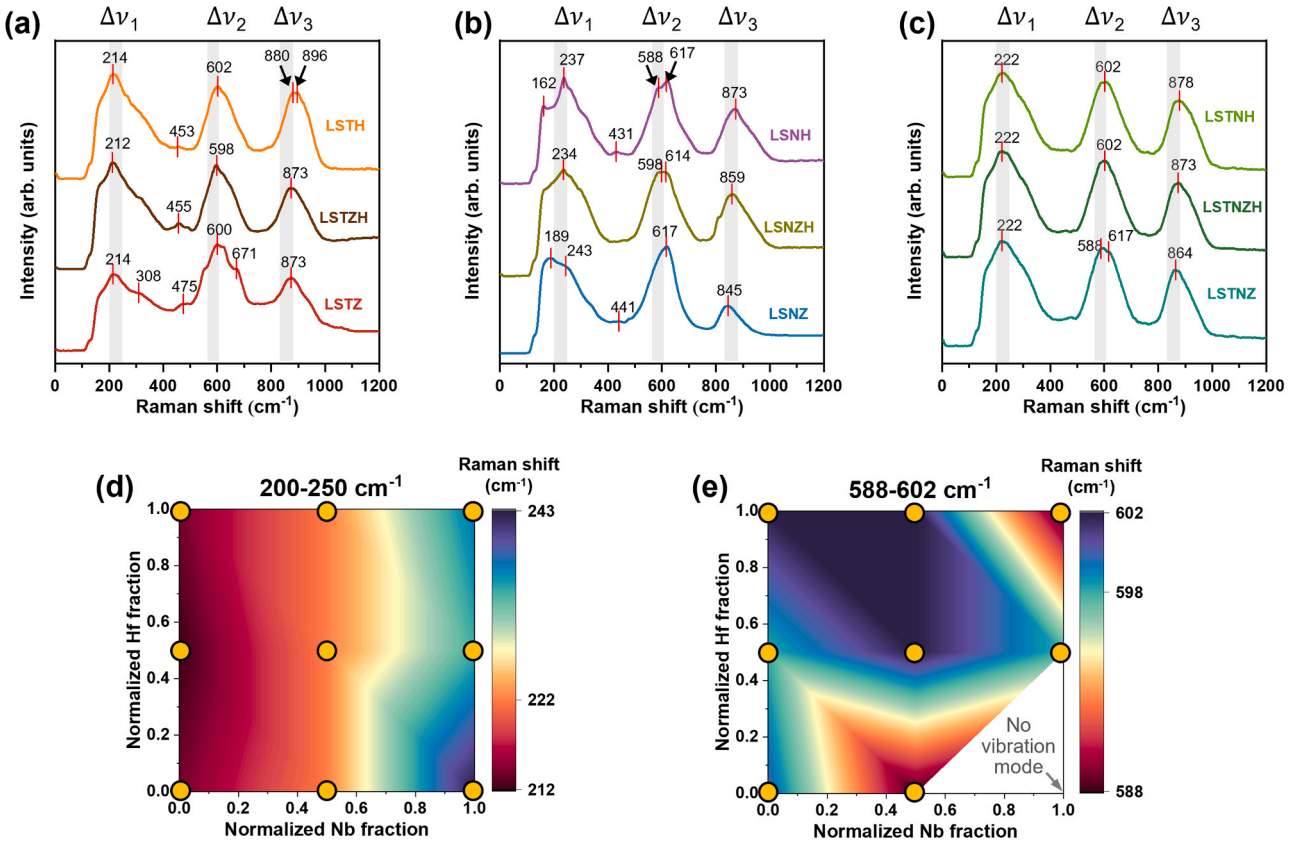

Fig. 5. Raman spectra of the (a) Ta-rich, (b) Nb-rich, and (c) mixed Nb-Ta groups in the Raman shift range of 0–1200 cm^{-1}. The major peaks are labeled as (i) $\Delta\nu_1$ at 200–250 cm^{-1}, (ii) $\Delta\nu_2$ at 588–602 cm^{-1}, and (iii) $\Delta\nu_3$ at 845–880 cm^{-1}. Raman shifts of (d) $\Delta\nu_1$ and (e) $\Delta\nu_2$ in the spectra in (a-c) for nine perovskite oxides correlated to the composition space, defined by normalized Nb fraction and normalized Hf fraction. The experimental data points are marked as filled circles in yellow and the colormap represents the lowest shift value (dark red) to the highest shift value (dark blue). LSNZ is excluded in (e) because of the missing vibration mode.

in the range of 300–500 cm^{-1} are likely related to vibrations caused by various impurities, particularly in LSTZ, which shows the lowest purity level of 93.57 %. The peak splitting near $\Delta\nu_2$ is observed in LSNH, LSNZH, and LSTNZ, which indicates the break of symmetry. The broad band at 800 cm^{-1} may correspond to the cation order-disorder band (A_{1g} mode), which is typically observed in complex perovskites, as reported for $Sr(Mg_{1/3}Nb_{2/3})O_3$, $La(Mg_{1/2}Ti_{1/2})O_3$, and $CaTiO_3$-$CaZrO_3$ solid solutions, when the multiple B-site cations with different charges are present [63].

Fig. 5(d) and (e) further display the relationship between the change in Raman shifts ($\Delta\nu_1$ and $\Delta\nu_2$) and B-site stoichiometry. The vibration mode, $\Delta\nu_1$, in the 200–250 cm^{-1} is associated with A- and B-site cations, which displays a monotonic shift towards higher wavenumber with the increase of the Nb fraction, although the peak shift values are independent of the Hf fraction (Fig. 5(d)). This implies the stronger off-center distortion ability of Nb^{5+} amongst d^0 transition metal cations ($Nb^{5+} > Ta^{5+} \gg Zr^{4+} \approx Hf^{4+}$). The change in the second major vibration mode, in the 588–602 cm^{-1} range, may involve both bending and stretching modes of BO_6, as shown in Fig. 5(e). LSTH, LSTNH, and LSTNZH exhibit the greatest distortions at similar levels, potentially due to Jahn-Teller distortions [56], but the change in distortion is not directly governed by the distortion ability of the B-site cations. For comparison, the octahedral factor is another empirical method to evaluate the tendency of B-cation moving away from octahedron sites to the other sites with higher or lower coordination numbers (CN), induced by dissimilar sizes of B-cations and anions [64–68]. For a perovskite based on the chemical formula, ABO_3, the octahedral factor, μ, is defined as:

$$\mu = \overline{r_B}/r_O, \tag{1}$$

where $\overline{r_B}$ are the averaged B-cation ionic radii weighted by mole fraction, and r_O is the ionic radius of oxygen. According to the reported geometric limits of perovskites [66], μ should be greater than 0.414, the octahedral limit, where oxygens in BO_6 are in contact with one another and each of them in contact with B-cations. The calculated octahedral factors shown in Fig. S4 follow the monotonic decrease trend with Hf substitution ($r_{Hf^{4+}}$: 0.71Å *vs.* $r_{Zr^{4+}}$: 0.72Å at CN = 6), depending solely on the slight decrease of averaged B-site ionic radii, independent of Nb substitution. With Hf substitution, $\overline{r_B}$ becomes smaller, pushing μ towards the octahedral limit, where the B-site cation has higher tendency of deviating from BO_6 center to accommodate the geometry change, consistent with general change in Raman shift in 588–602 cm^{-1} towards a high Hf^{4+} fraction.

Despite the subtle size difference among B-site cations, their electron configuration difference should be considered, which changes B-O bond strength and phonon frequency [69]. Based on the effect of B-site Zr and Hf substitution in tungsten bronze [70], it has been shown that Hf-O bonds are more ionic with less covalency than Zr-O bonds. The higher ionization energy of Hf leads to exponential increase in phonon frequency, which indicates stronger bond strength of Hf-O than Zr-O bonds [69]. Likewise, Ta-O exhibits less covalency than Nb-O bonds [70]. The stronger B-O bonds are favorable for fast ion transports in lattice [5], which are consistent with our findings of increase in bulk ionic conductivity as compositions increase in Hf and Ta fractions (Fig. 4(f)). Given the above discussion, lattice expansion and distortion are not only influenced by ionic radii differences, but also by electron configuration differences, coupling effects from cation species and sublattices, and changes in BO_6 bonding, all of which contribute to determining ion mobility in the bulk. In short, the total ionic conductivity is not only affected by microstructures, but also influenced by the crystal structure at the unit cell level.

Fig. 6 illustrates the correlations between composition variables (y, z) and key descriptors for the six samples sintered at 1300°C, from the Ta-rich group ($y = 0$) and the mixed Nb-Ta group ($y = 0.5$). This analysis eliminates the influence of the sintering temperature (1200°C for the Nb-rich group, due to partial melting at 1300°C) on the microstructures. The selected descriptors include microstructure features (including phase purity, relative density, and grain size), crystal structure descriptors (including lattice constant, Raman shift, and octahedral factor), and ionic transport properties (including σ_{bulk}, σ_{gb}, σ_{gb}^{spec}, and σ_{total}). The Pearson correlation coefficient (PCC) of two variables (a, b) is computed as [71,72]:

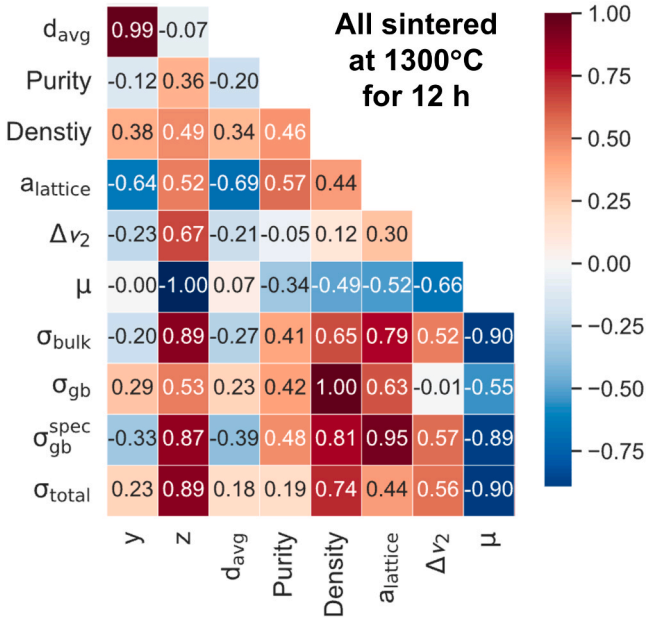

Fig. 6. Pearson correlation coefficients of the Ta-rich and mixed Nb-Ta groups (all sintered as the same temperature) on compositional variables (y and z) and key measured microstructural features and properties, including mean grain size (d_{avg}), phase purity, relative density, lattice constant ($a_{lattice}$), Raman shift at 588–602 cm^{-1} ($\Delta\nu_2$), octahedral factor (μ), bulk ionic conductivity (σ_{bulk}), apparent GB ionic conductivity (σ_{gb}), specific GB ionic conductivity (σ_{gb}^{spec}), and total ionic conductivity (σ_{total}). The positive correlation is represented by red color, while the negative correlation is represented by blue color.

$$r_{ab} = \frac{\sum_{i=1}^{n}(a_i - \overline{a})(b_i - \overline{b})}{\sqrt{\sum_{i=1}^{n}(a_i - \overline{a})^2}\sqrt{\sum_{i=1}^{n}(b_i - \overline{b})^2}} \tag{2}$$

where n represents sample size ($n = 6$); a_i and b_i are sample points of (a, b) variables that satisfy $(a, b) \in \{d_{avg},\ purity,\ density,\ \ldots,\ \sigma_{total}\}$. $r = 1$ indicates a perfect positive correlation (dark red in Fig. 6), while $r = -1$ means a perfect negative correlation (dark blue in Fig. 6). To justify the confidence level of the correlations, the P value and hypothesis testing is performed. The P value stands for the probability of two variables with no significant correlations where the null hypothesis is true [73]. When the P value is smaller than the pre-chosen significance level of 0.05, the correlations are statistically significant. The heatmaps of P values and PCC with $P < 0.05$ are shown in Fig. S5. For a statistically significant correlation, PCC value is greater than 0.60 or lower than −0.60.

On the one hand, the composition variable y (*i.e.*, the normalized Nb^{5+} fraction or $X_{Nb}/(X_{Nb} + X_{Ta})$) shows a strong positive correlation with the mean grain size (PCC = 0.99), as the substitution of Nb promotes grain growth. The refractory nature of Ta, however, reduces the grain growth promotion. Additionally, y has a slight positive correlation (PCC = 0.29) with σ_{gb}, but exhibit negative correlation (PCC = −0.33) with σ_{gb}^{spec}. This indicates that Nb addition reduces σ_{gb}^{spec}, while it promotes grain growth, thereby increasing the total σ_{gb} (due to a lower fraction of GBs with increasing grain size). If we consider all data shown in Supporting Fig. S6(a), overall σ_{total} reduces with the increasing fraction of Nb (PCC = −0.51). Lastly, the composition variable y is

negatively correlated with the lattice constant, indicating a higher Nb^{5+} fraction results in a smaller lattice constant.

On the other hand, the composition variable z (the normalized Hf^{4+} fraction or $X_{Hf}/(X_{Hf} + X_{Zr})$) is negatively correlated with octahedral factor (μ) and positively correlated with bulk, specific GB, and total ionic conductivity (σ_{bulk}, σ_{gb}^{spec}, and σ_{total}). The higher X_{Hf} (or lower X_{Zr}) results in the decrease in $\overline{r_B}$ and μ, while σ_{bulk}, σ_{gb}^{spec}, σ_{total} get promoted. The increase in bulk ionic conductivity is related to the larger lattice constant and greater lattice distortion, which is also validated in the positive correlation of z with Raman shift at Peak 2 ($\Delta\nu_2$), as a higher Hf^{4+} fraction results in stronger B-O bond strength and more BO_6 octahedral distortion. The positive correlations between compositional variable z (the normalized Hf fraction) and the ionic conductivities suggests that Hf addition increases σ_{bulk}, σ_{gb}^{spec}, and σ_{total} overall.

The cross-correlations among different types of variables are also observed in Fig. 6. For instance, the positive correlation pairs include density with σ_{bulk}, σ_{gb}, and σ_{gb}^{spec}, or σ_{total}, and $a_{lattice}$ with σ_{bulk}, σ_{gb} and σ_{gb}^{spec}. These correlations can be well explained. First, the high relative density yields less pores in bulk and intimate contacts between grains, which promotes ionic conduction in general. Second, the larger lattice constant results in larger bottleneck size for ion conduction. Considering all data in Supporting Fig. S6(c), $\Delta\nu_2$ also shows positive correlation with σ_{bulk} and σ_{total}. The larger Raman shift indicates greater lattice distortion, contributing to higher σ_{bulk} and σ_{total}. With regard to the negatively correlated pairs, σ_{bulk}, σ_{gb}^{spec}, and σ_{total} increase as octahedral factor decreases. The change in σ_{gb}^{spec} may result from the change in bulk chemistry, which further affects GB chemistry. Overall, higher density, larger lattice constant, larger Raman shift, and smaller octahedral factor are beneficial for higher ionic conductivity. Further studies are needed to investigate the exact underlying mechanisms of these correlations.

3.4. *Nb effects on the processing-microstructure-interface-property relationship*

The observed grain growth promotion and sintering enhancement associated with Nb_2O_5 addition can also result in changes in grain boundaries and secondary phases. To investigate the possible mechanism, we characterize the microstructures and GBs (including interfacial precipitation that affects both sintering and GB resistance) in LSNZH and LSTZH for a direct comparison of Nb-rich and Ta-rich CCPOs (Fig. 7). Fig. 7(a-c) presents the backscattered electron images and elemental distribution in LSNZH at low and high magnifications from SEM. The dark contrast surrounding grains represents the presence of lighter elements, which is confirmed as a Nb-rich GB precipitation phase in the EDS maps in Fig. 7(c), as well as Supporting Fig. S7 and Fig. S8. We perform high-resolution EBSD at the GB triple junction and verify the GB precipitates are $LiNbO_3$-based phase, shown in Supporting Fig. S9. This result implies GB wetting, possibly by a low-melting-point $LiNbO_3$-based liquid, which results in interfacial precipitation of Nb-rich secondary phase in cooled specimens.

To confirm the phase decomposition, the EDS elemental quantification (Supporting Fig. S10 and Table S4) at the primary phase region indicates the primary phase is Sr-enriched with an approximate stoichiometric formula as $Sr_{0.5}(Nb_{0.8}Zr_{0.1}Hf_{0.1})O_{2.9}$, whereas the composition of GB secondary phase is estimated as $(Li_{0.012}Sr_{0.221})(Nb_{0.857}Zr_{0.070}Hf_{0.074})O_{2.655}$ by considering the overall charge balance between cations and oxygens. It is inferred that the stoichiometric LSNZH (a $4 \times 2 \times 2$ supercell $Li_6Sr_7Nb_{12}Zr_2Hf_2O_{48}$) decomposes into $3Li_2SrNb_2O_7$, $2SrNb_2O_6$, $Sr_2Nb_2O_7$ and $4(Hf_{0.5}Z_{0.5})O_2$, where $3Li_2SrNb_2O_7$ can be further decomposes into $6LiNbO_3$ and 3SrO. Therefore, $LiNbO_3$ and $SrNb_2O_6$ at a ratio of 3:1 is approximately identical to the eutectic composition of $LiNbO_3$-$SrNb_2O_6$ binary phase diagram [74]. The liquid phase forms above 1170°C, which explains the formation of $LiNbO_3$ precipitates along GBs as an indication of liquid phase sintering and GB-wetting promoted grain growth [75,76]. In contrast, no precipitation is evident in Nb-free LSTZH and the element distribution is homogeneous (Fig. 7(d-f)).

To understand the role of Nb in regulating atomic-scale structure and compositions, we used aberration-corrected scanning transmission electron microscopy (AC STEM) in combination with EDS to investigate both the crystal structures (grains of the bulk phase as well as secondary phases) and GBs of LSNZH and LSTZH. Fig. 8(a, b) show representative HAADF-STEM images of the primary phase (perovskite) and a common secondary phase, (Hf, Zr)O_2.

Since the secondary phases made up 2.84 % by area in LSNZH, quantified by EBSD phase map (Supporting Fig. S11), phase boundaries were investigated. Fig. 8(c) shows a HAADF-STEM image and corresponding EDS elemental maps of a phase boundary formed by primary phase LSNZH (perovskite, right grain) and secondary phase (Hf, Zr)O_2 (left grain). By tilting the left grain to a low-index zone axis, Supporting

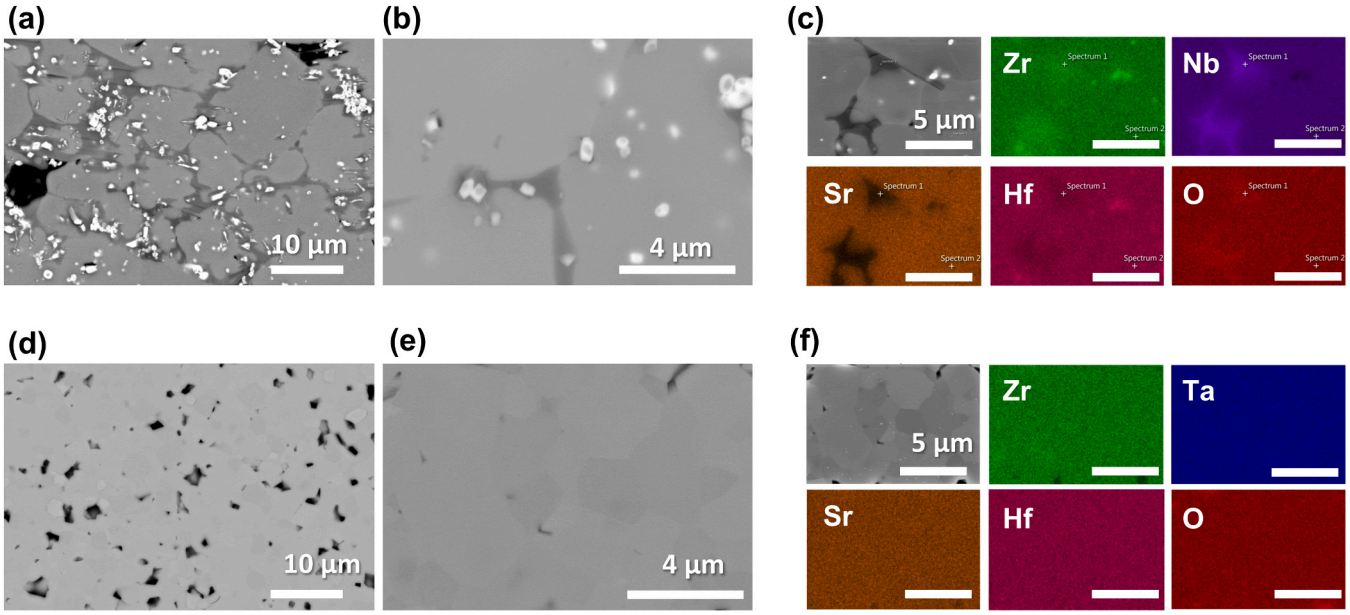

Fig. 7. The backscattered electron SEM images and EDS elemental maps of (a-c) LSNZH and (d-f) LSTZH. The scale bars are 5 μm in (c) and (f).

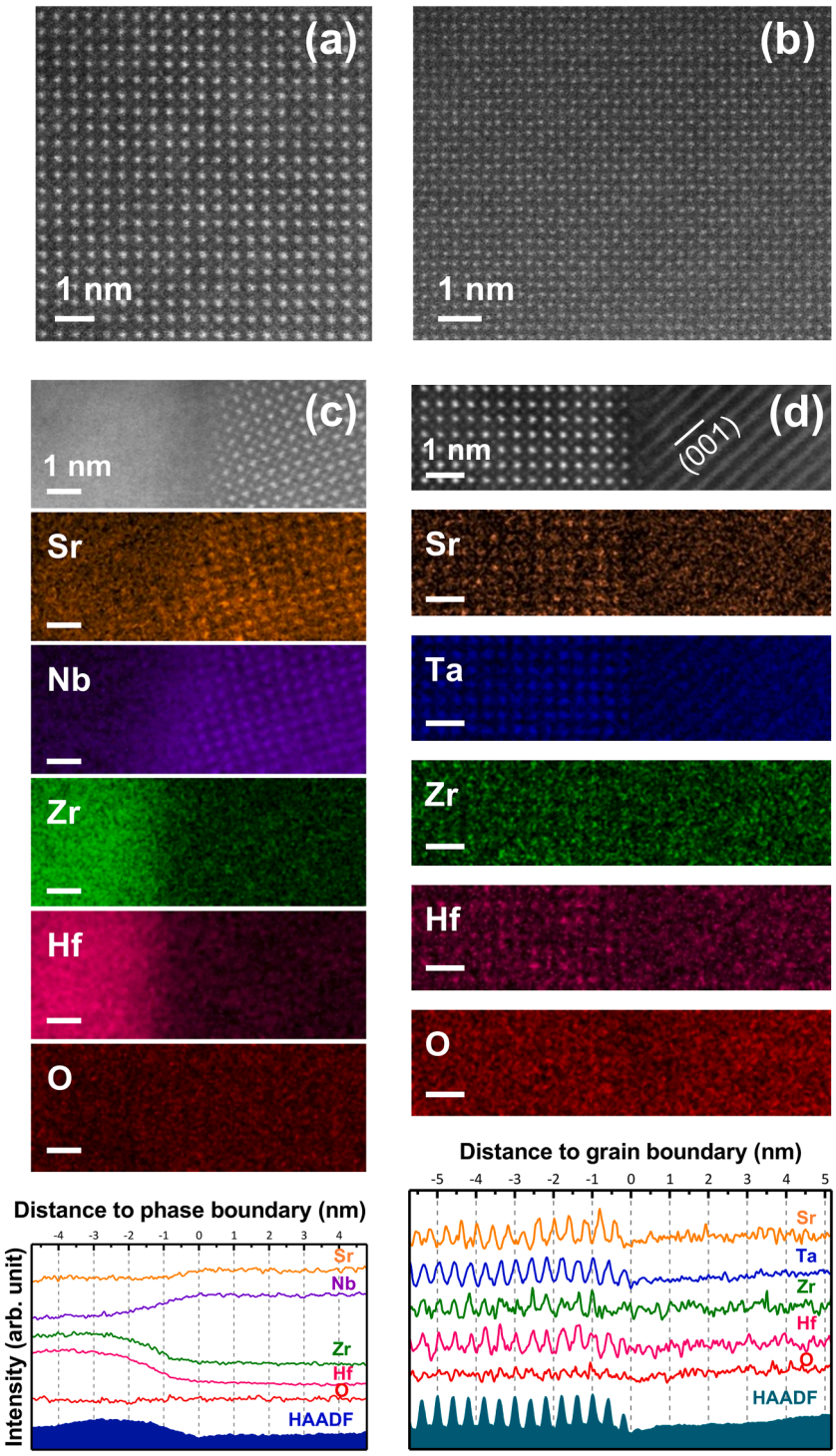

Fig. 8. (a-b) Atomic resolution HAADF-STEM images of (a) the regular, disordered perovskite and (b) the monoclinic $Hf_{0.5}Zr_{0.5}O_2$ secondary phase found in the LSNZH TEM specimen. Both grains in (a) and (b) are in [100] zone axes. (c) Atomic resolution HAADF-STEM image of a phase boundary found in LSNZH. The grain on the right is cubic perovskite LSNZH in [100] zone axis, while the grain on the left is orthorhombic $Hf_{0.5}Zr_{0.5}O_2$ in a high-index zone axis. Intensity profiles of EDS elemental and HAADF signals are shown at the bottom of panel (c). (d) Atomic resolution HAADF-STEM image and elemental maps of a GB found in LSTZH. The grain on the left is in [100] zone axis. Intensity profiles of EDS elemental and HAADF signals are shown at the bottom of panel (d). All scale bars are 1 nm.

Fig. S12(a) shows that the secondary phase is orthorhombic (space group $Pbc2_1$). To further analyze this phase boundary, EDS spectra were collected. Atomic-resolution elemental maps of Sr, Nb, Zr, Hf, and O are generated using intensities from Sr-K, Nb-K, Zr-K, Hf-L, and O-K edges and are shown in Fig. 8(c). A plot of vertically integrated intensity profiles of the HAADF image and elemental maps is also shown at the bottom in Fig. 8(c). From 0 nm to ~ − 2.75 nm in distance to the phase boundary (*x*-axis), a gradual increase in HAADF intensity is observed. Correlating with this increase, the Zr and Hf intensities gradually increase while the Sr and Nb intensities gradually decrease. From − 2.75 nm to − 4 nm in distance to the phase boundary, the HAADF intensity gradually decreases, correlating with the further decrease in Nb intensity, while Sr, Zr, and Hf signals remain constant. Since the HAADF-STEM image intensity is dictated by the average atomic number

($Z_{average}$) of the elements present [77], it is reasonable that the (Hf, Zr)O_2 ($Z_{average}$ = 24) grain appears brighter than the LSNZH ($Z_{average} \approx 18$) grain. The high Zr and Hf signals observed in the left grain corroborate with our finding from Supporting Fig. S12(a) that this grain is hafnium-zirconium oxide. More importantly, the two effects secondary phases have on the primary phase are clear. First, they result in a gradual change in composition near the phase boundary (0 nm to − 4 nm in distance to the phase boundary). This interphase as well as the secondary phases themselves would result in large interfacial resistance, which is accounted for by the GB component appearing in frequency lower than the "grain bulk" component in Nyquist plots. Though in our LSNZH Nyquist plot, only one arc is observed; thus, the GB component cannot be fitted. Second, these secondary phases will cause the composition of the primary phase to deviate from the nominal $(Li_{0.375}Sr_{0.4375})(Nb_{0.75}Zr_{0.125}Hf_{0.125})O_{3-\delta}$. Consequently, the low σ_{total} of LSNZH is attributed to its secondary phases.

Having revealed the origin of poor ionic conductivity in LSNZH, we investigated the Nb-free composition of LSTZH as a comparison. This composition is the only one that contained no Nb and has a σ_{total} close to those of LSTNZ and LSTNH. Fig. 8(d) displays an atomic resolution HAADF-STEM image and corresponding EDS elemental maps of a GB of LSTZH. Following the same analysis applied to LSNZH, EDS spectra were collected at the GB. Atomic-resolution elemental maps of Sr, Ta, Zr, Hf, and O are generated using intensities from Sr-K, Ta-L, Zr-K, Hf-L, and O-K edges and are shown in Fig. 8(d). A plot of vertically integrated intensity profiles of the HAADF image and elemental maps is also shown at the bottom in Fig. 8(d). At the GB, a decrease in image intensity that correlates well with the decrease in intensity of Sr, Ta, Zr, and Hf is revealed. This indicates that this GB contains more Sr, Ta, Zr, and Hf vacancies than the grain bulk. From the HAADF-STEM image, we see the same crystal lattices extend all the way from the bulk to the GB, indicating the crystal structure of GB resembles that of a defective cubic perovskite. This finding is similar to the results previously reported on LSTZ and air-quenched LSTNZH [8,26], though no obvious elemental segregation is found, and the fraction of vacancies observed here appears less.

We note that the specific GB conductivity (σ_{gb}^{spec}) of LSTNZ is comparable to that of LSTZH, which are both around 10^{-6} S/cm. Based on these results, it is possible that LSTNZ will have GB structures similar to those in LSTZH. The change in σ_{gb}^{spec} on 2D compositional space is shown in Supporting Fig. S13(a). The difference in total ionic conductivities between LSTZH and LSTNZ are mainly related to microstructure-level features. For instance, the smaller mean grain size (1.47 μm) and the poorer sintering density (87.52 %) in LSTZH lead to lower apparent GB ionic conductivity of 0.217 mS/cm (*vs.* 0.656 mS/cm of LSTNZ) (Fig. 3(h) and Table 2). From the direct comparison of LSTZH and LSNZH pair, we can conclude that the phase instability and the subsequent GB wetting by $LiNbO_3$ change the GB structures and enhance grain growth but constrain the total ionic conductivity. With the half substitution of Nb in LSTNZ, LSTNH and LSTNZH, the detrimental effect from $LiNbO_3$ formation is suppressed and the single phase is stabilized with enlarged grain sizes and excess vacancies at GBs, which can increase the total ionic conductivities. LSTNH, especially, exhibits the highest total ionic conductivity of 0.336 mS/cm among all five newly reported CCPOs, potentially originating from the greatest structural distortion induced by Hf substitution and changing B-O bonding, along with mixed a Ta-Nb composition achieve a balance in phase stability and grain growth. The contour map of total ionic conductivity (Fig. S13(b)) is correlated to that of Raman shift around 600 cm^{-1} (Fig. 5(b)), which further justifies our postulation.

4. Conclusions

In this work, we investigated the effects of B-site cation chemistry of CCPOs in 2D compositional space on microstructural evolution, structural expansion/distortion (change in lattice constants and Raman shift), and interfaces, which impact on Li-ion conduction in the bulk phase and through interfaces. After investigating the composition-microstructure-property relation in a matrix of nine specimens in the 2D compositional space, we show that good total ionic conductivity can be attained in medium-entropy CCPO LSTNH or $(Li_{0.375}Sr_{0.4375})(Ta_{0.375}Nb_{0.375}Hf_{0.25})O_{3-\delta}$ with three different cations mixed on the B site through a synergy of multiple effects that are tuned by two independent compositional variables (y and z). First, Nb cations promote sintering and grain growth, thereby eliminating pores and resistive GBs, while the perovskite phase is stabilized by the addition of Ta cations, so that a balance is achieved at $y = 0.5$. Second, the lattice is expanded by Hf cations to open the bottleneck for ion transport, so that high ionic conductivity is achieved at $z = 1$. In addition, Raman spectroscopy suggests that the BO_6 octahedral distortion is maximized in LSTNH (similar to the distortion levels in LSTH and LSTNZH), contributing to enhanced ion transport in the bulk phase. Through the examination of correlations among composition, structure and microstructure, and ionic conduction, we identify the role of different B-site cations in affecting properties.

The need for simultaneous optimization of crystal structures (lattice constants and distortion) and microstructures justifies the investigation of a 2D compositional space in non-equimolar CCPOs. In general, the demands for simultaneous optimization of multiple structural and microstructural features and properties calls for the exploration of medium- and high-entropy CCCs in multidimensional compositional spaces, particularly non-equimolar compositions. However, maximizing entropy for CCCs are generally not necessary. For example, $(Li_{0.375}Sr_{0.4375})(Ta_{0.375}Nb_{0.375}Hf_{0.25})O_{3-\delta}$ discovered in this study outperforms their higher-entropy counterpart, $(Li_{0.375}Sr_{0.4375})(Ta_{0.375}Nb_{0.375}Hf_{0.125}Zr_{0.125})O_{3-\delta}$, which was the best-performed composition in the most recent first report of CCPO solid electrolytes [26], thereby representing an advancement from the prior state of the art.

CRediT authorship contribution statement

Shyue Ping Ong: Writing – review & editing, Investigation, Formal analysis. **Jose Arturo Venegas:** Investigation, Data curation. **Tom Lee:** Writing – original draft, Visualization, Methodology, Investigation, Formal analysis, Data curation. **Shu-Ting Ko:** Writing – original draft, Visualization, Validation, Methodology, Investigation, Formal analysis, Data curation, Conceptualization. **Jian Luo:** Writing – review & editing, Visualization, Validation, Supervision, Resources, Project administration, Methodology, Investigation, Funding acquisition, Formal analysis, Conceptualization. **Xiaoqing Pan:** Supervision, Resources, Project administration, Methodology, Investigation, Formal analysis.

Declaration of Competing Interest

The authors declare that they have no known competing financial interests or personal relationships that could have appeared to influence the work reported in this paper.

Acknowledgements

This research was primarily supported by the National Science Foundation (NSF) Materials Research Science and Engineering Center (MRSEC) program through the UC Irvine Center for Complex and Active Materials (Grant DMR-2011967). This work used shared research facilities at the San Diego Nanotechnology Infrastructure (SDNI) of University of California San Diego (UCSD), a member of the National Nanotechnology Coordinated Infrastructure, which is supported by the NSF (Grant ECCS-2025752), UCSD MRSEC shared instrumentation (NSF Grant DMR-2011924), UCSD Nanoengineering Materials Research Center (NE-MRC), and the Irvine Materials Research Institute (also

supported in part by the NSF Grant DMR-2011967).

Appendix A. Supporting information

Supplementary data associated with this article can be found in the online version at doi:10.1016/j.jeurceramsoc.2024.117126.

References

[1] S. Randau, D.A. Weber, O. Kötz, R. Koerver, P. Braun, A. Weber, E. Ivers-Tiffée, T. Adermann, J. Kulisch, W.G. Zeier, F.H. Richter, J. Janek, Benchmarking the performance of all-solid-state lithium batteries, Nat. Energy 5 (3) (2020) 259–270, https://doi.org/10.1038/s41560-020-0565-1.

[2] J. Janek, W.G. Zeier, A solid future for battery development, Nat. Energy 1 (9) (2016) 16141, https://doi.org/10.1038/nenergy.2016.141.

[3] A. Manthiram, X. Yu, S. Wang, Lithium battery chemistries enabled by solid-state electrolytes, Nat. Rev. Mater. 2 (4) (2017) 16103, https://doi.org/10.1038/natrevmats.2016.103.

[4] R. Wei, S. Chen, T. Gao, W. Liu, Challenges, fabrications and horizons of oxide solid electrolytes for solid-state lithium batteries, Nano Sel. 2 (12) (2021) 2256–2274, https://doi.org/10.1002/nano.202100110.

[5] S. Stramare, V. Thangadurai, W. Weppner, Lithium lanthanum titanates: a review, Chem. Mater. 15 (21) (2003) 3974–3990, https://doi.org/10.1021/cm0300516.

[6] C. Chen, Ionic conductivity, lithium insertion and extraction of lanthanum lithium titanate, Solid State Ion. 144 (1-2) (2001) 51–57, https://doi.org/10.1016/S0167-2738(01)00884-0.

[7] H. Yang, N. Wu, Ionic conductivity and ion transport mechanisms of solid-state lithium-ion battery electrolytes: a review, Energy Sci. Eng. 10 (5) (2022) 1643–1671, https://doi.org/10.1002/ese3.1163.

[8] T. Lee, J. Qi, C.A. Gadre, H. Huyan, S.-T. Ko, Y. Zuo, C. Du, J. Li, T. Aoki, R. Wu, J. Luo, S.P. Ong, X. Pan, Atomic-scale origin of the low grain-boundary resistance in perovskite solid electrolyte $Li_{0.375}Sr_{0.4375}Ta_{0.75}Zr_{0.25}O_3$, Nat. Commun. 14 (1) (2023) 1940, https://doi.org/10.1038/s41467-023-37115-6.

[9] C. Chen, Stable lithium-ion conducting perovskite lithium–strontium–tantalum–zirconium–oxide system, Solid State Ion. 167 (3-4) (2004) 263–272, https://doi.org/10.1016/j.ssi.2004.01.008.

[10] A. Sarkar, B. Breitung, H. Hahn, High entropy oxides: the role of entropy, enthalpy and synergy, Scr. Mater. 187 (2020) 43–48, https://doi.org/10.1016/j.scriptamat.2020.05.019.

[11] J.W. Yeh, S.K. Chen, S.J. Lin, J.Y. Gan, T.S. Chin, T.T. Shun, C.H. Tsau, S.Y. Chang, Nanostructured high-entropy alloys with multiple principal elements: novel alloy design concepts and outcomes, Adv. Eng. Mater. 6 (5) (2004) 299–303, https://doi.org/10.1002/adem.200300567.

[12] M.C. Gao, D.B. Miracle, D. Maurice, X. Yan, Y. Zhang, J.A. Hawk, High-entropy functional materials, J. Mater. Res. 33 (19) (2018) 3138–3155, https://doi.org/10.1557/jmr.2018.323.

[13] M. Botros, J. Janek, Embracing disorder in solid-state batteries, Science 378 (6626) (2022) 1273–1274, https://doi.org/10.1126/science.adf3383.

[14] Z. Lun, B. Ouyang, D.-H. Kwon, Y. Ha, E.E. Foley, T.-Y. Huang, Z. Cai, H. Kim, M. Balasubramanian, Y. Sun, J. Huang, Y. Tian, H. Kim, B.D. McCloskey, W. Yang, R.J. Clément, H. Ji, G. Ceder, Cation-disordered rocksalt-type high-entropy cathodes for Li-ion batteries, Nat. Mater. 20 (2) (2021) 214–221, https://doi.org/10.1038/s41563-020-00816-0.

[15] R. Zhang, C. Wang, P. Zou, R. Lin, L. Ma, L. Yin, T. Li, W. Xu, H. Jia, Q. Li, S. Sainio, K. Kisslinger, S.E. Trask, S.N. Ehrlich, Y. Yang, A.M. Kiss, M. Ge, B.J. Polzin, S. J. Lee, W. Xu, Y. Ren, H.L. Xin, Compositionally complex doping for zero-strain zero-cobalt layered cathodes, Nature 610 (7930) (2022) 67–73, https://doi.org/10.1038/s41586-022-05115-z.

[16] Q. Wang, A. Sarkar, D. Wang, L. Velasco, R. Azmi, S.S. Bhattacharya, T. Bergfeldt, A. Düvel, P. Heitjans, T. Brezesinski, H. Hahn, B. Breitung, Multi-anionic and -cationic compounds: New high entropy materials for advanced Li-ion batteries, Energy Environ. Sci. 12 (8) (2019) 2433–2442, https://doi.org/10.1039/C9EE00368A.

[17] K. Wang, W. Hua, X. Huang, D. Stenzel, J. Wang, Z. Ding, Y. Cui, Q. Wang, H. Ehrenberg, B. Breitung, C. Kübel, X. Mu, Synergy of cations in high entropy oxide lithium ion battery anode, Nat. Commun 14 (1) (2023) 1487, https://doi.org/10.5445/IR/1000154295.

[18] H. Chen, N. Qiu, B. Wu, Z. Yang, S. Sun, Y. Wang, A new spinel high-entropy oxide $(Mg_{0.2}Ti_{0.2}Zn_{0.2}Cu_{0.2}Fe_{0.2})_3O_4$ with fast reaction kinetics and excellent stability as an anode material for lithium ion batteries, RSC Adv. 10 (16) (2020) 9736–9744, https://doi.org/10.1039/D0RA00255K.

[19] B. Ouyang, Y. Zeng, The rise of high-entropy battery materials, Nat. Commun. 15 (1) (2024) 973, https://doi.org/10.1038/s41467-024-45309-9.

[20] M.J. Deck, Y.-Y. Hu, Leveraging local structural disorder for enhanced ion transport, J. Mater. Res. 38 (10) (2023) 2631–2644, https://doi.org/10.1557/s43578-023-01023-8.

[21] J. Lin, G. Cherkashinin, M. Schäfer, G. Melinte, S. Indris, A. Kondrakov, J. Janek, T. Brezesinski, F. Strauss, A high-entropy multicationic substituted lithium argyrodite superionic solid electrolyte, ACS Mater. Lett. 4 (11) (2022) 2187–2194, https://doi.org/10.1021/acsmaterialslett.2c00667.

[22] Y.-Y. Hu, (Invited) Entropy-enhanced ion transport in solid electrolytes. ECS Meeting Abstracts, IOP Publishing, 2021, pp. 443-443.

[23] S. Jiang, T. Hu, J. Gild, N. Zhou, J. Nie, M. Qin, T. Harrington, K. Vecchio, J. Luo, A new class of high-entropy perovskite oxides, Scr. Mater. 142 (2018) 116–120, https://doi.org/10.1016/j.scriptamat.2017.08.040.

[24] A.J. Wright, Q. Wang, S.-T. Ko, K.M. Chung, R. Chen, J. Luo, Size disorder as a descriptor for predicting reduced thermal conductivity in medium- and high-entropy pyrochlore oxides, Scr. Mater. 181 (2020) 76–81, https://doi.org/10.1016/j.scriptamat.2020.02.011.

[25] D. Zhang, H.A. De Santiago, B. Xu, C. Liu, J.A. Trindell, W. Li, J. Park, M. A. Rodriguez, E.N. Coker, J.D. Sugar, A.H. McDaniel, S. Lany, L. Ma, Y. Wang, G. Collins, H. Tian, W. Li, Y. Qi, X. Liu, J. Luo, Compositionally complex perovskite oxides for solar thermochemical water splitting, Chem. Mater. 35 (5) (2023) 1901–1915, https://doi.org/10.1021/acs.chemmater.2c03054.

[26] S.-T. Ko, T. Lee, J. Qi, D. Zhang, W.-T. Peng, X. Wang, W.-C. Tsai, S. Sun, Z. Wang, W.J. Bowman, S.P. Ong, X. Pan, J. Luo, Compositionally complex perovskite oxides: discovering a new class of solid electrolytes with interface-enabled conductivity improvements, Matter 6 (7) (2023) 2395–2418, https://doi.org/10.1016/j.matt.2023.05.035.

[27] K.M. Ok, P.S. Halasyamani, D. Casanova, M. Llunell, P. Alemany, S. Alvarez, Distortions in octahedrally coordinated d^0 transition metal oxides: a continuous symmetry measures approach, Chem. Mater. 18 (14) (2006) 3176–3183, https://doi.org/10.1021/cm0604817.

[28] R. Yu, Q.-X. Du, B.-K. Zou, Z.-Y. Wen, C.-H. Chen, Synthesis and characterization of perovskite-type (Li,Sr)(Zr,Nb)O_3 quaternary solid electrolyte for all-solid-state batteries, J. Power Sources 306 (2016) 623–629, https://doi.org/10.1016/j.jpowsour.2015.12.065.

[29] B. Huang, B. Xu, Y. Li, W. Zhou, Y. You, S. Zhong, C.-A. Wang, J.B. Goodenough, Li-ion conduction and stability of perovskite $Li_{3/8}Sr_{7/16}Hf_{1/4}Ta_{3/4}O_3$, ACS Appl. Mater. Interfaces 8 (23) (2016) 14552–14557, https://doi.org/10.1021/acsami.6b03070.

[30] Y. Kong, Y. Li, J. Lu, Influence of sintering aids and excess Lithium on the conductivity of perovskite-type $Li_{3/8}Sr_{7/16}Zr_{1/4}Nb_{3/4}O_3$ solid electrolyte, Ceram. Int. 43 (7) (2017) 5642–5646, https://doi.org/10.1016/j.ceramint.2017.01.097.

[31] Y. Kong, Y. Li, J. Lu, C. Hu, Conductivity and electrochemical stability of perovskite-structured lithium–strontium–niobium–hafnium-oxide solid Li-ion conductors, J. Mater. Sci.: Mater. Electron. 28 (12) (2017) 8621–8629, https://doi.org/10.1007/s10854-017-6586-2.

[32] R. Inada, K. Kimura, K. Kusakabe, T. Tojo, Y. Sakurai, Synthesis and lithium-ion conductivity for perovskite-type $Li_{3/8}Sr_{7/16}Ta_{3/4}Zr_{1/4}O_3$ solid electrolyte by powder-bed sintering, Solid State Ion.-. 261 (2014) 95–99, https://doi.org/10.1016/j.ssi.2014.04.005.

[33] R. Ruh, P.W.R. Corfield, Crystal structure of monoclinic hafnia and comparison with monoclinic zirconia, J. Am. Ceram. Soc. 53 (3) (1970) 126–129, https://doi.org/10.1111/j.1151-2916.1970.tb12052.x.

[34] S.C. Abrahams, J.L. Bernstein, Ferroelectric lithium tantalate—1. single crystal X-ray diffraction study at 24°C, J. Phys. Chem. Solids 28 (9) (1967) 1685–1692, https://doi.org/10.1016/0022-3697(67)90142-4.

[35] T. Kolodiaznyi, H. Sakurai, M. Isobe, Y. Matsushita, S. Forbes, Y. Mozharivskyj, T.J. S. Munsie, G.M. Luke, M. Gurak, D.R. Clarke, Superconductivity and crystal structural origins of the metal-insulator transition in $Ba_{6-x}Sr_xNb_{10}O_{30}$ tetragonal tungsten bronzes, Phys. Rev. B 92 (21) (2015) 214508, https://doi.org/10.1103/PhysRevB.92.214508.

[36] G.W.J.C. Heunen, D.J.W. Ijdo, R.B. Helmholdt, $SrTa_4O_{11}$: a rietveld refinement using neutron powder diffraction data, Acta Crystallogr. Sect. C: Cryst. Struct. Commun. 51 (9) (1995) 1723–1725, https://doi.org/10.1107/S0108270195004264.

[37] T. Siegrist, R.J. Cava, J.J. Krajewski, Reduced alkaline earth tantalates, Mater. Res. Bull. 32 (7) (1997) 881–887, https://doi.org/10.1016/S0025-5408(97)00066-4.

[38] W. Rheinheimer, E. Schoof, M. Selzer, B. Nestler, M.J. Hoffmann, Non-Arrhenius grain growth in strontium titanate: quantification of bimodal grain growth, Acta Mater. 174 (2019) 105–115, https://doi.org/10.1016/j.actamat.2019.05.040.

[39] W. Rheinheimer, M.J. Hoffmann, Grain growth transitions of perovskite ceramics and their relationship to abnormal grain growth and bimodal microstructures, J. Mater. Sci. 51 (4) (2016) 1756–1765, https://doi.org/10.1007/s10853-015-9535-6.

[40] A. Sharafi, C.G. Haslam, R.D. Kerns, J. Wolfenstine, J. Sakamoto, Controlling and correlating the effect of grain size with the mechanical and electrochemical properties of $Li_7La_3Zr_2O_{12}$ solid-state electrolyte, J. Mater. Chem. A 5 (40) (2017) 21491–21504, https://doi.org/10.1039/C7TA06790A.

[41] J.C.C. Abrantes, J.A. Labrincha, J.R. Frade, Applicability of the brick layer model to describe the grain boundary properties of strontium titanate ceramics, J. Eur. Ceram. Soc. 20 (10) (2000) 1603–1609, https://doi.org/10.1016/S0955-2219(00)00022-4.

[42] J. Fleig, J. Maier, The impedance of ceramics with highly resistive grain boundaries: validity and limits of the brick layer model, J. Eur. Ceram. Soc. 19 (6-7) (1999) 693–696, https://doi.org/10.1016/S0955-2219(98)00298-2.

[43] S.M. Haile, D.L. West, J. Campbell, The role of microstructure and processing on the proton conducting properties of gadolinium-doped barium cerate, J. Mater. Res. 13 (6) (1998) 1576–1595, https://doi.org/10.1557/JMR.1998.0219.

[44] B. Huang, S. Zhong, J. Luo, Z. Huang, C.A. Wang, Highly dense perovskite electrolyte with a high Li^+ conductivity for Li–ion batteries, J. Power Sources 429 (2019) 75–79, https://doi.org/10.1016/j.jpowsour.2019.04.117.

[45] S.J. Dillon, M.P. Harmer, Diffusion controlled abnormal grain growth in ceramics, Mater. Sci. Forum 558-559 (2007) 1227–1236, https://doi.org/10.4028/www.scientific.net/MSF.558-559.1227.

[46] H. Salama, K. Marquardt, J. Kundin, O. Shchyglo, I. Steinbach, The role of grain boundary energy anisotropy on the grain size evolution during normal grain growth Motivation, EGU General Assembly 2020, EGU2020-21694, Online, 2020.
[47] H. Salama, J. Kundin, O. Shchyglo, V. Mohles, K. Marquardt, I. Steinbach, Role of inclination dependence of grain boundary energy on the microstructure evolution during grain growth, Acta Mater. 188 (2020) 641–651, https://doi.org/10.1016/j.actamat.2020.02.043.
[48] P.E. Goins, W.E. Frazier, A model of grain boundary complexion transitions and grain growth in Yttria-doped alumina, Acta Mater. 188 (2020) 79–91, https://doi.org/10.1016/j.actamat.2019.12.061.
[49] P. Du, N. Li, X. Ling, Z. Fan, A. Braun, W. Yang, Q. Chen, A. Yelon, Optimizing the proton conductivity with the isokinetic temperature in perovskite-type proton conductors according to Meyer–Neldel rule, Adv. Energy Mater. 12 (5) (2022) 2102939, https://doi.org/10.1002/aenm.202102939.
[50] S. Palakkathodi Kammampata, H. Yamada, T. Ito, R. Paul, V. Thangadurai, The activation entropy for ionic conduction and critical current density for Li charge transfer in novel garnet-type $Li_{6.5}La_{2.9}A_{0.1}Zr_{1.4}Ta_{0.6}O_{12}$ (A = Ca, Sr, Ba) solid electrolytes, J. Mater. Chem. A 8 (5) (2020) 2581–2590, https://doi.org/10.1039/C9TA12193E.
[51] A.C. Moy, G. Häuschen, D. Fattakhova-Rohlfing, J.B. Wolfenstine, M. Finsterbusch, J. Sakamoto, The effects of aluminum concentration on the microstructural and electrochemical properties of lithium lanthanum zirconium oxide, J. Mater. Chem. A 10 (41) (2022) 21955–21972, https://doi.org/10.1039/D2TA03676B.
[52] T. Wen, Y. Jin, J. Yu, Z. Yan, Z. Liu, L. Yuan, Effect of Nb_2O_5 additive on the sintering behavior and properties of calcium hexaluminate, Constr, Build. Mater. 385 (2023) 131534, https://doi.org/10.1016/j.conbuildmat.2023.131534.
[53] M.P. Chorney, K. Mondal, J.P. Downey, P.K. Tripathy, On the sintering behavior of Nb_2O_5 and Ta_2O_5 mixed oxide, powders,Materials 15 (14) (2022) 5036, https://doi.org/10.3390/ma15145036.
[54] R.S. Roth, L.W. Coughanour, Phase equilibrium relations in the systems titania-niobia and zirconia-niobia, J, Res. Natl. Bur. Stand. 55 (4) (1955) 209, https://doi.org/10.6028/JRES.055.023.
[55] K. Kim, D.J. Siegel, Correlating lattice distortions, ion migration barriers, and stability in solid electrolytes, J. Mater. Chem. A 7 (7) (2019) 3216–3227, https://doi.org/10.1039/C8TA10989C.
[56] M.W. Lufaso, P.M. Woodward, Jahn–Teller distortions, cation ordering and octahedral tilting in perovskites, Acta Crystallogr. Sect. B: Struct. Sci. 60 (1) (2004) 10–20, https://doi.org/10.1107/S0108768103026661.
[57] M.C. Weber, J. Kreisel, P.A. Thomas, M. Newton, K. Sardar, R.I. Walton, Phonon Raman scattering of RCrO3 perovskites (R=Y, La, Pr, Sm, Gd, Dy, Ho, Yb, Lu), Phys. Rev. B 85 (5) (2012) 054303, https://doi.org/10.1103/PhysRevB.85.054303.
[58] B. Mihailova, U. Bismayer, B. Güttler, M. Gospodinov, L. Konstantinov, Local structure and dynamics in relaxor-ferroelectric $PbSc_{1/2}Nb_{1/2}O_3$ and $PbSc_{1/2}Ta_{1/2}O_3$ single crystals, J. Phys.: Condens. Matter 14 (5) (2002) 1091–1105, https://doi.org/10.1088/0953-8984/14/5/314.
[59] A.B.S. Lavinscky, A.-M. Welsch, B.J. Kennedy, M.I.B. Bernardi, V.R. Mastelaro, Order-disorder phenomena and octahedral tilting in $SrTi_{1-x}Sn_xO_3$ perovskites – a structural and spectroscopic study, J. Solid State Chem. 269 (2019) 521–531, https://doi.org/10.1016/j.jssc.2018.10.006.
[60] D. Michel, M.P. y Jorba, R. Collongues, Study by Raman spectroscopy of order-disorder phenomena occurring in some binary oxides with fluorite-related structures, J. Raman Spectrosc. 5 (2) (1976) 163–180, https://doi.org/10.1002/jrs.1250050208.
[61] G. Keresztury, Raman spectroscopy: theory, in: J. Chalmers, P. Griffith (Eds.), Handbook of Vibrational Spectroscopy, John Wiley & Sons, New York, 2002, pp. 71–87.
[62] S.K. Jaiswal, Investigation on phase and Raman spectra of $Ba_3(CaTa_{2-y}Ti_y)O_{9-\delta}$ (y = 0 – 0.50) system, J. Asian Ceram. Soc. 8 (3) (2020) 572–577, https://doi.org/10.1080/21870764.2020.1786914.
[63] H. Zheng, I.M. Reaney, G.D.C.C. De Györgyfalva, R. Ubic, J. Yarwood, M.P. Seabra, V.M. Ferreira, Raman spectroscopy of $CaTiO_3$-based perovskite solid solutions, J. Mater. Res. 19 (2) (2004) 488–495, https://doi.org/10.1557/jmr.2004.19.2.488.
[64] V.M. Goldschmidt, Die gesetze der krystallochemie, Naturwissenschaften 14 (21) (1926) 477–485, https://doi.org/10.1007/BF01507527.
[65] C.J. Bartel, C. Sutton, B.R. Goldsmith, R. Ouyang, C.B. Musgrave, L.M. Ghiringhelli, M. Scheffler, New tolerance factor to predict the stability of perovskite oxides and halides, Sci. Adv. 5 (2) (2019) eaav0693, https://doi.org/10.1126/sciadv.aav0693.
[66] M.R. Filip, F. Giustino, The geometric blueprint of perovskites, Proc. Natl. Acad. Sci. U. S. A. 115 (21) (2018) 5397–5402, https://doi.org/10.1073/pnas.1719179115.
[67] D. Ji, S. Feng, L. Wang, S. Wang, M. Na, H. Zhang, C. Zhang, X. Li, Regulatory tolerance and octahedral factors by using vacancy in $APbI_3$ perovskites, Vacuum 164 (2019) 186–193, https://doi.org/10.1016/j.vacuum.2019.03.018.
[68] T. Duan, I. Mora-Seró, Y. Zhou, Introduction to perovskite, in: Y. Zhou, I. Mora Seró (Eds.), Halide Perovskite Semiconductors, John Wiley & Sons, New Jersey, 2024, pp. 1–8.
[69] M.K. Shamim, G.M. Kale, S. Sardar, D.N. Singh, S. Sharma, A.K. Yadav, S.N. Jha, D. Bhattacharyya, R.J. Choudhary, Effect of B-site cationic substitution on the structural, spectroscopic, and conductivity behaviour of $Ho_2(Hf_{1-x}Zr_x)_2O_7$ (x=0 and 1), Ceram. Int. 50 (9) (2024) 16404–16411, https://doi.org/10.1016/j.ceramint.2024.02.125.
[70] W. Feng, S. Long, Y. Wan, D. Zhang, Effect of B-site Zr and Hf substitution on ferroelectric polar order for tetragonal tungsten bronze ceramic, J. Asian Ceram. Soc. 10 (2) (2022) 396–404, https://doi.org/10.1080/21870764.2022.2062809.
[71] J. Benesty, J. Chen, Y. Huang, I. Cohen, Pearson correlation coefficient, in: J. Benesty, W. Kellermann (Eds.), Noise Reduction in Speech Processing, Springer, Berlin, Heidelberg, 2009, pp. 1–4.
[72] J.J. Berman, Understanding your data, Data Simplification: Taming Information With Open Source Tools, Morgan Kaufmann, Boston, 2016, pp. 135-187.
[73] E. Komaroff, Relationships between p-values and Pearson correlation coefficients, type 1 errors and effect size errors, under a true null hypothesis, J. Stat. Theory Pract 14 (3) (2020) 49, https://doi.org/10.1007/s42519-020-00115-6.
[74] D.-S. Tang, J.-K. Liang, T.-J. Shi, Y.-L. Zhang, J.-H. Tian, W.-X. Li, Investigation of the pseudo-ternary system $SrNb_2O_6$-$NaNbO_3$-$LiNbO_3$, Acta. Phys. Sin 28 (1) (1979) 62, https://doi.org/10.7498/aps.28.62.
[75] B.B. Straumal, A.A. Mazilkin, B. Baretzky, Grain boundary complexions and pseudopartial wetting, Curr. Opin. Solid State Mater. Sci. 20 (5) (2016) 247–256, https://doi.org/10.1016/j.cossms.2016.05.006.
[76] W. Rheinheimer, M. Bäurer, M.J. Hoffmann, A reversible wetting transition in strontium titanate and its influence on grain growth and the grain boundary mobility, Acta Mater. 101 (2015) 80–89, https://doi.org/10.1016/j.actamat.2015.08.069.
[77] S.J. Pennycook, Z-contrast transmission electron microscopy: direct atomic imaging of materials, Annu. Rev. Mater. Sci. 22 (1) (1992) 171–195, https://doi.org/10.1146/annurev.ms.22.080192.001131.